Engineering Geology 293 (2021) 106288

Contents lists available at ScienceDirect

Engineering Geology

journal homepage: www.elsevier.com/locate/enggeo

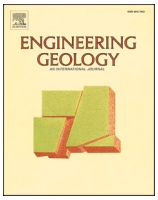

Landslide size matters: A new data-driven, spatial prototype

Luigi Lombardo [a,*], Hakan Tanyas [b,c], Raphaël Huser [d], Fausto Guzzetti [e,f], Daniela Castro-Camilo [g]

[a] University of Twente, Faculty of Geo-Information Science and Earth Observation (ITC), PO Box 217, Enschede, AE 7500, Netherlands
[b] Hydrological Sciences Laboratory, NASA Goddard Space Flight Center, Greenbelt, MD, United States
[c] USRA, Universities Space Research Association, Columbia, MD, United States
[d] King Abdullah University of Science and Technology (KAUST), Computer, Electrical and Mathematical Sciences and Engineering (CEMSE) Division, Thuwal 23955-6900, Saudi Arabia
[e] Consiglio Nazionale delle Ricerche (CNR), Istituto di Ricerca per la Protezione Idrogeologica (IRPI), via Madonna Alta 126, 06128 Perugia, Italy
[f] Presidenza del Consiglio dei Ministri, Dipartimento della Protezione Civile, via Vitorchiano 2, 00189 Roma, Italy
[g] School of Mathematics and Statistics, University of Glasgow, Glasgow G12 8QQ, UK

ARTICLE INFO

Keywords:
Integrated nested Laplace approximation (INLA)
Landslide hazard
Earthquake
Landslide area prediction
Slope unit
Bayesian spatial modelling

ABSTRACT

The standard definition of landslide hazard requires the estimation of where, when (or how frequently) and how large a given landslide event may be. The geoscientific community involved in statistical models has addressed the component pertaining to how large a landslide event may be by introducing the concept of landslide-event magnitude scale. This scale, which depends on the planimetric area of the given population of landslides, in analogy to the earthquake magnitude, has been expressed with a single value per landslide event. As a result, the geographic or spatially-distributed estimation of how large a population of landslide may be when considered at the slope scale, has been disregarded in statistically-based landslide hazard studies. Conversely, the estimation of the landslide extent has been commonly part of physically-based applications, though their implementation is often limited to very small regions.

In this work, we initially present a review of methods developed for landslide hazard assessment since its first conception decades ago. Subsequently, we introduce for the first time a statistically-based model able to estimate the planimetric area of landslides aggregated per slope units. More specifically, we implemented a Bayesian version of a Generalized Additive Model where the maximum landslide size per slope unit and the sum of all landslide sizes per slope unit are predicted via a Log-Gaussian model. These "max" and "sum" models capture the spatial distribution of (aggregated) landslide sizes. We tested these models on a global dataset expressing the distribution of co-seismic landslides due to 24 earthquakes across the globe. The two models we present are both evaluated on a suite of performance diagnostics that suggest our models suitably predict the aggregated landslide extent per slope unit. In addition to a complex procedure involving variable selection and a spatial uncertainty estimation, we built our model over slopes where landslides triggered in response to seismic shaking, and simulated the expected failing surface over slopes where the landslides did not occur in the past.

What we achieved is the first statistically-based model in the literature able to provide information about the extent of the failed surface across a given landscape. This information is vital in landslide hazard studies and should be combined with the estimation of landslide occurrence locations. This could ensure that governmental and territorial agencies have a complete probabilistic overview of how a population of landslides could behave in response to a specific trigger. The predictive models we present are currently valid only for the 25 cases we tested. Statistically estimating landslide extents is still at its infancy stage. Many more applications should be successfully validated before considering such models in an operational way. For instance, the validity of our models should still be verified at the regional or catchment scale, as much as it needs to be tested for different landslide types and triggers. However, we envision that this new spatial predictive paradigm could be a breakthrough in the literature and, in time, could even become part of official landslide risk assessment protocols.

* Corresponding author.
E-mail address: l.lombardo@utwente.nl (L. Lombardo).

https://doi.org/10.1016/j.enggeo.2021.106288
Received 18 January 2021; Received in revised form 15 May 2021; Accepted 16 July 2021
Available online 24 July 2021

1. Introduction

Landslides are common in the mountains, in the hills, and along high costs, where they can pose serious threats to the population, public and private properties, and the economy (Kennedy et al., 2015; Petley, 2012; Daniell et al., 2017; Broeckx et al., 2019). To cope with the landslide problem (Brabb, 1991; Nadim et al., 2006), and in an attempt to mitigate the landslide damaging effects through proper land planning (Kockelman, 1986; Brabb and Harrod, 1989; Glade et al., 2005), investigators have long attempted to map landslides (Guzzetti et al., 2012; Mondini et al., 2021), to quantify landslide susceptibility (Reichenbach et al., 2018), intensity (Lombardo et al., 2018b, 2019b, 2020a), and hazard (Varnes and the IAEG Commission on Landslides and Other Mass-Movements, 1984; Guzzetti et al., 1999; Fell et al., 2008; Lari et al., 2014), to evaluate the vulnerability to landslides of various elements at risk (Fuchs et al., 2007; Galli and Guzzetti, 2007; van Westen et al., 2008), including the population (Dowling and Santi, 2014; Pereira et al., 2017; Salvati et al., 2018), and to ascertain landslide risk, qualitatively (Fell and Harford, 1997, 1997; Reichenbach et al., 2005; Glade et al., 2005) or quantitatively (Salvati et al., 2010; Corominas et al., 2014; Rossi et al., 2019).

A problem with many of these attempts has always been the inability (or at least the difficulty) to measure and predict the size—*i.e.*, depth, length, width, area, volume, and their multiple ratios and dependencies (Dai and Lee, 2001; Malamud et al., 2004b; Brunetti et al., 2009a; Guzzetti et al., 2009; Taylor et al., 2018a)—of the landslides, which are known to measure, control, or influence landslide magnitude (Keefer, 1984; Cardinali et al., 2002; Fuchs et al., 2007), impact (Guzzetti et al., 2003; Bout et al., 2018; van den Bout et al., 2021), and destructiveness (Fell and Harford, 1997; Cardinali et al., 2002), which in turn depend on the landslide types (Hungr et al., 2014). In this work, we propose an innovative approach to build statistical models capable of predicting the planimetric area of event-triggered landslides (Stark and Hovius, 2001; Malamud et al., 2004b; Guzzetti et al., 2012). To test the approach, we construct and validate two models that predict metrics related to the planimetric area of earthquake-induced landslides (EQILs) (Keefer, 1984, 2013). For the purpose, we exploit the information on the geographical location and planimetric area of 319,086 landslides shown in 25 EQIL inventories available from the global database collated by Schmitt et al. (2017) and Tanyaş et al. (2017)—currently the largest and most comprehensive repository of information on seismically-triggered slope failures, globally (Fan et al., 2019)—together with spatial morphometric and environmental variables in the areas covered by the 25 EQIL inventories, and on the seismic properties of the triggering earthquakes.

The manuscript is organized as follows. We begin by giving background information on the inherent difficulty to predict landslide sizes, including landslide area or other simple geometric measures of landslide size (Section 2). Next, we provide the theoretical background for our statistical models, and of the metrics that we selected to measure the performance of our models (Section 4). This is followed by a presentation of the data used to construct and validate our models, including the target and explanatory variables, and of the adopted terrain mapping unit (Section 3). Next, we compare the results of our modelling effort (Section 5) and we discuss the model outputs in view of their specific and general relevance, and we provide considerations on the impact of our approach for the modelling of landslide hazard (Section 6). We conclude summarizing the lessons learnt, with a perspective towards possible future research.

2. Background

Varnes and the IAEG Commission on Landslides and Other Mass-Movements (1984) were the first to define landslide hazard as "*the probability of occurrence within a specified period of time and within a given area of a potentially damaging landslide*" (Fell et al., 2008). This definition originated from the more general one used by the United Nations Disaster Relief Organization (UNDRO) for all-natural hazards, which in turn was a generalization of the definition used for seismic hazard (National Research Council, 1991). Fifteen years later, Guzzetti et al. (1999) extended the definition to include the magnitude of the expected landslide, and landslide hazard became "*the probability of occurrence within a specified period of time and within a given area of a potentially damaging landslide of a given magnitude*". Today, this remains the most common and generally accepted definition of landslide hazard.

A problem with this definition is that, in contrast to other natural hazards—including, *e.g.*, earthquakes (Wood and Neumann, 1931; Gutenberg and Richter, 1936), volcanic eruptions (Newhall and Self, 1982), hurricanes (Saffir, 1973; Simpson, 1974), floods (Buchanan and Somers, 1976)—no unique measure or scale for landslide magnitude exists (Hungr, 1997a; Malamud et al., 2004b; Guzzetti, 2005). This complicates the practical application of the definition (Guzzetti, 2005). A further complication arises from the use of the same term "landslide" to address both the landslide deposit (*i.e.*, the failed mass) and the movement of slope materials or of an existing landslide mass (Cruden, 1991; Guzzetti, 2005).

In the literature, different approaches and metrics were proposed to size or rank the "magnitude" of a single landslide, or a population of landslides—*i.e.*, a number of landslides in a given area resulting from a single event or multiple events in a period (Malamud et al., 2004b; Rossi et al., 2010). For single landslides, authors have proposed to measure landslide "magnitude" using the size (*e.g.*, area, depth, volume) (Fell, 1994; Cardinali et al., 2002; Reichenbach et al., 2005), velocity (UNESCO Working Party On World Landslide Inventory, 1995; Cruden and Varnes, 1996; Hungr et al., 2014), kinetic energy (Ksu, 1975; Sassa, 1988; Corominas and Mavrouli, 2011), or destructiveness (Hungr, 1997b; Reichenbach et al., 2005; Galli and Guzzetti, 2007) of the slope failure. Alternatively, Cardinali et al. (2002) and Reichenbach et al. (2005) proposed to size landslide magnitude based on an empirical relation linking landslide volume and velocity, a proxy for momentum. Other possible metrics that can be used to measure the magnitude of a single landslide include, *e.g.*, the depth of the landslide mass, the total or the differential ground displacement caused by the landslide, the discharge per unit width (for landslides of the flow type), or the momentum of the failed mass. This type of kinematic characteristics may be better suited to inform on the landslide hazard compared to landslides' area of volume (Corominas et al., 2014). For instance, a large deep-seated slowly-moving landslide may pose a negligible threat compared to a small rockfall. In fact, the high velocity of the rockfall could lead to a much larger hazard to local communities or infrastructure. However, no data of landslide dynamics (*e.g.*, kinetic energy) are currently available for large populations of landslides, making the landslide area the only directly measurable property for large inventories.

A few authors have established empirical probability distributions of landslide size (or measures thereof) including, *e.g.*, area (Stark and Hovius, 2001; Guzzetti et al., 2002; Malamud et al., 2004b; Korup et al., 2011; Chen et al., 2017; Jacobs et al., 2017), volume (Martin et al., 2002; Dussauge et al., 2003; Malamud et al., 2004b; Brunetti et al., 2009b), area-to-volume (Guzzetti et al., 2009; Larsen et al., 2010; Tang et al., 2019), and width-to-length (Parise and Jibson, 2000; Rickli et al., 2009; Taylor et al., 2018b) ratios. Moreover, a few authors have examined the factors controlling these distributions (*e.g.*, Pelletier et al., 1997; Guthrie and Evans, 2004; Stark and Guzzetti, 2009; Frattini and Crosta, 2013; Korup et al., 2012; Williams et al., 2018; Tanyaş et al., 2019b; Jeandet et al., 2019; Bellugi et al., 2021). Some of the established distributions were used to estimate landslide magnitude for hazard assessment at the catchment scale, where the probability of landslide area $p(A_L)$, was taken to represent landslide magnitude, *e.g.*, by Guzzetti et al. (2005, 2006). However, the use of empirical probability distributions of measures of landslide size has several problems. First, to establish reliable distributions of, *e.g.*, landslide area or volume, one

needs large numbers of empirical data, which can only be obtained from large and accurate landslide event inventory maps. These data are not common and difficult, time-consuming, and costly to prepare (Malamud et al., 2004b; Guzzetti et al., 2012; Mondini et al., 2021). Second, although Malamud et al. (2004b) and Malamud et al. (2004a) have argued that their Inverse Gamma distribution, and other similar distributions (Stark and Hovius, 2001; Hovius et al., 1997), are general ("universal"), and do not depend on the local terrain or the triggering conditions, the hypothesis was challenged by, *e.g.*, Korup et al. (2011) and Tanyaş et al. (2018). It is not clear the extent to which a single distribution holds outside the geographical area where it was defined. Third, even the availability of reliable empirical distributions of landslide area or volume does not guarantee that the estimates obtained from the distribution are accurate in all parts of the study area where it was defined, and specifically in all slopes and sections of a complex landscape. Fourth, lack of standard methods and tools to properly model the probability distributions of landslide sizes hampers the possibility to confront empirical distributions obtained for different areas or the same area at different times (Rossi et al., 2012).

To the best of our knowledge, no model able to capture and predict the spatial distribution of landslide sizes (or measures thereof) has been proposed in the literature. However, for co-seismic landslides, few examples do exist where scholars have at least tried to estimate the controlling factors of landslide size. The most common observation points out to a possible relation between distance to rupture zone and landslide size (*e.g.*, Keefer and Manson, 1998; Khazai and Sitar, 2004; Massey et al., 2018; Valagussa et al., 2019). This implies that larger landslides are expected to be closer to the fault zone where the influence of ground motion is more intense. In fact, Medwedeff et al. (2020) indicated that the contribution of ground motion has a limited control on size of the landslides, compared to hillslope relief. Another common observation suggests that extremely large landslides can be generally associated with structural features (*e.g.*, Chigira and Yagi, 2006; Catani et al., 2016). Such features cannot be taken into account in regional multivariate analysis because of limited data regarding the discontinuity surfaces (Fan et al., 2019). Other investigators emphasise the control of ground-motion characteristics (*e.g.*, frequency content, duration) on landslide size (*e.g.*, Bourdeau et al., 2004; Jibson et al., 2004, 2020; Kramer, 1996; Valagussa et al., 2019). For example, Jibson and Tanyaş (2020) demonstrated a positive correlation between landslide size and magnitude, ground motion duration, and mean period. These hypotheses require further analyses which need strong-motion records gathered from a very dense accelerometer monitoring network. Nevertheless, we lack such spatial detail to examine available earthquake-triggered landslide events. This may be the reason why even just explanatory models for landslide sizes are so limited in numbers.

Typical, statistically-based, spatially-distributed landslide predictive models attempt to identify "where" landslides may occur in a given region based on a set of environmental characteristics known to control, or condition landslide occurrence, or their lack of occurrence (Reichenbach et al., 2018). These susceptibility models explain the discrete, presence/absence of landslides in any given terrain mapping unit, be it, *e.g.*, a grid cell, a unique condition unit, a slope unit (SU), or any other terrain subdivision. For this purpose, the models exploit the Bernoulli probability distribution to describe the presence/absence (1/0) of landslides (Reichenbach et al., 2018). Therefore, in this context, the size of the landslides in each terrain mapping unit is irrelevant.

Recently, Lombardo et al. (2018b) have proposed to estimate the landslide intensity, an alternative measure complementary to landslide susceptibility, describing the expected number of landslides in any given terrain mapping unit. To estimate this intensity measure spatially over large and very large areas, the authors built statistically-based, spatially-distributed predictive models that adopt the Poisson probability distribution to explain the discrete number (0, 1, 2, 3, …) of landslides in any given terrain mapping unit. Moreover, Lombardo et al. (2020a) have shown that the landslide intensity is positively correlated with the landslide area, explaining a large portion of its variability within slope units. Nevertheless, as for susceptibility models, the actual size of the landslides in each mapping unit is irrelevant for the implementation of intensity models, and such models cannot predict the size (*e.g.*, the area or volume) of the landslides.

In this work, we extend the traditional approaches used to estimate landslide susceptibility, and the more recent approach proposed to estimate landslide intensity, to model the size (area) of the landslides in any given terrain mapping unit in a landscape. For this purpose, we build statistically-based, spatially-distributed predictive models that adopt the log-Gaussian probability distribution to explain characteristics related to the (aggregated) area of landslides in each mapping unit, namely

- A_{Lmax}, the largest landslide in the considered terrain mapping unit; and
- A_{Lsum}, the sum of all landslide areas in the considered terrain mapping unit.

Further details on how A_{Lmax} and A_{Lsum} have been extracted from our dataset is provided in Sections 3.1 and 3.4, whereas a description of how these have been modelled is provided in Section 4.

3. Data

To test our modelling framework, we used information on (i) the location and the planimetric area of a large number of landslides caused by earthquakes of different magnitudes in various parts of the world; (ii) the morphometric and environmental settings in the same areas where the EQILs were triggered; and (iii) on the ground shaking conditions caused by the earthquakes that triggered the EQILs. In addition, we selected a type of terrain subdivision into mapping units known to be suited to model and predict landslides spatially.

3.1. Earthquake-induced landslide data

We obtained information on EQILs searching the largest collection (link here) of seismically-induced landslide event inventories currently available (Schmitt et al., 2017; Tanyaş et al., 2017). At the time of the search (March 2019), this unique source contained cartographic and thematic information on 64 EQIL inventories caused by 46 earthquakes that occurred between 1971 and 2016 globally, counting 554, 333 landslides (Fig. 1). To select the inventories best suited for the scope of our work, we adopted two criteria. First, an inventory must have contained information on the (planimetric) area of each of the mapped landslides. Second, the landslides shown in the inventory must have been associated with an earthquake for which ground motion data were available from the U.S. Geological Survey (USGS) ShakeMap system (Worden and Wald, 2016). Applying the two criteria, we selected 25 EQIL inventories in the 40-year period between 1976 and 2016, which collectively encompass 319,086 landslides in 25 study areas in 13 nations, in all continents, except Oceania and Antarctica, and in a broad range of morphological, geological, tectonic, seismic, and climate settings (Fig. 1 and Table S1).

With the exception of the 2007 Pisco, Peru, inventory (see Fig. 1 and ID 14 in Table S1), prepared using a combination of automated classification and manual adjustment techniques (Lacroix et al., 2013), all the selected inventories were obtained through the systematic, visual interpretation of satellite images and/or aerial photography (Tanyaş et al., 2017). For 23 out of the 25 EQIL inventories, showing a total of 303, 269 landslides (95.0% of the total number of landslides), landslides were mapped as polygons, and the planimetric area of each landslide, A_L, in m^2, was calculated in a GIS. For 22 of these inventories, the polygon showing an individual landslide typically encompasses (*i.e.*, it does not separate) the landslide source and deposition areas. Only for the 2015 Gorkha, Nepal, inventory (see Fig. 1 and ID 24 in Table S1) the

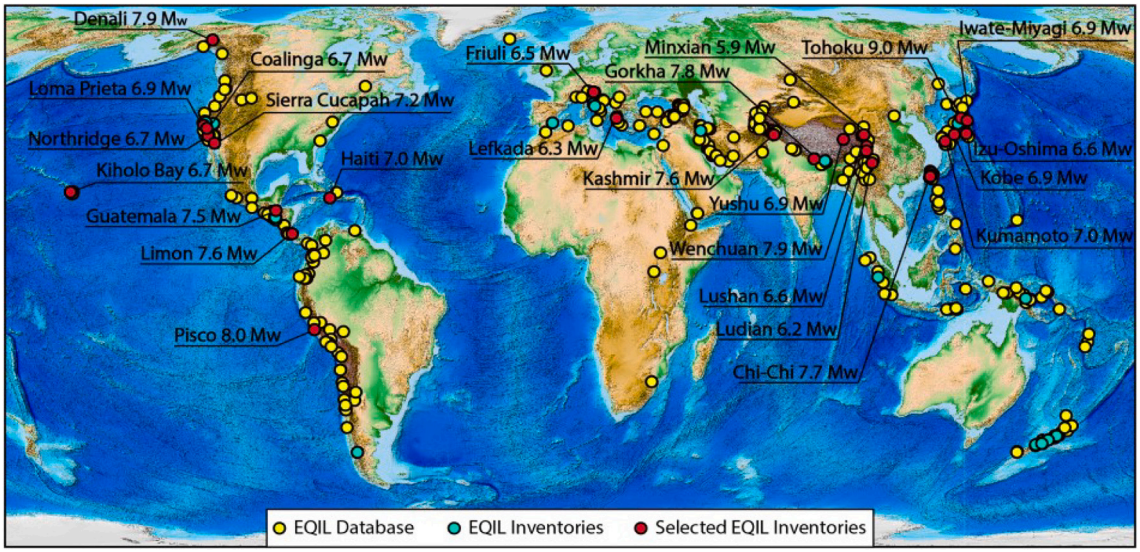

Fig. 1. Map shows locations (yellow dots) of all the earthquakes known to have triggered landslides and reported in the co-seismic landslide database collated by Schmitt et al. (2017) and Tanyaş et al. (2017) publicly available (https://www.sciencebase.gov/catalog/item/583f4114e4b04fc80e3c4a1a). The cyan dots show all the earthquakes for which the database above includes one or more corresponding landslide inventories, out of which, the red dots represent the inventories used in this study. Map uses Equal Earth map projection (EPSG:2018.048, Šavrič et al., 2019). (For interpretation of the references to color in this figure legend, the reader is referred to the web version of this article.)

source and deposition areas of each landslide were shown separately (Roback et al., 2017). For this inventory, to obtain the landslide area A_L we merged the landslide source and deposition areas. In the 2007 Pisco, Peru (Lacroix et al., 2013) (271 landslides, 0.09%), and the 2013 Lushan, China (Xu et al., 2015) (see Fig. 1 and ID 21 in Table S1) (15, 546 landslides, 4.0%), inventories, landslides were shown as points, corresponding to the known, inferred, or assumed location of the landslide initiation point, with the landslide area listed in a joint, attribute table.

We would like to point out here that several sources of uncertainty may affect the measurement of landslide areas and further details on this topic will be described in depth in Section 6.3.

3.2. Terrain mapping unit

Among the several possible terrain mapping units used for spatial landslide modelling (Hansen, 1984; Soeters and van Westen, 1996; Guzzetti et al., 1999; Reichenbach et al., 2018), we selected the "slope units" (SUs), which are geomorphological and hydrological terrain subdivisions bounded by drainage and divide lines (Carrara, 1988; Alvioli et al., 2016). SUs represent a good geometric description of natural slopes, where most landslides occur. For our work, we exploited the same sets of SUs used previously by Tanyaş et al. (2019a) to model landslide susceptibility, and to predict the spatial occurrence of landslides, in the same 25 study areas. Tanyaş et al. (2019a) generated the SU terrain subdivisions for the study areas (Fig. 1) using *r.slopeunits*, an open source software for GRASS GIS (GRASS Development Team, 2017) developed by Alvioli et al. (2016) for the automatic partitioning of a landscape into SUs. Table S1 lists the main geometric characteristics of the 144, 724 SUs in the 25 study areas, which collectively cover 219, 010 km^2.

In consolidated methods to estimate the landslide susceptibility, intensity, and hazard (Reichenbach et al., 2018; Lombardo et al., 2018a; Guzzetti et al., 2005), binary datasets are built by assigning to each mapping unit a label indicating the presence/absence of landslides or their count. In this process, mapping units containing the information of slope failures are as important as mapping units where the instability has not been observed. As a result, a balanced (Marjanović et al., 2011) or unbalanced (Frattini et al., 2010; Lombardo and Mai, 2018) dichotomous dataset constitute the basic information upon which any following model is regressed. In our case, since we do not have to classify the SUs, but rather build a model on the basis of the landslide planimetric area, we are only interested in the SUs with mapped landslides, where the extent per mapping unit can be computed.

For this reason, from the initial set of 144, 724 SUs—representing all the mapping units combined across the 25 study areas, we extracted a subset of 23, 343 SUs (16.1%, for a total area of about 62, 794 km^2) where EQILs have been mapped reporting their planimetric extent. This subset represents the dataset upon which we will build our modelling protocol. As for the complementary subset made of 121, 661 SUs without known landslides—83.9%, for a total area of about 156, 216 km^2—we separately store this information for it will enter the whole procedure only as the prediction target (as explained in Section 4.4).

3.3. Morphometric, environmental, and seismic data

For our modelling, we used an initial set of morphometric, environmental, and ground shaking (seismic) data obtained from a variety of digital cartographic sources. The data we used can be grouped into three main classes, namely:

- terrain morphometric properties, which we obtained from the 1 arcsec × 1 arcsec (approximately, 30 m × 30 m, at the equator) SRTM Digital Elevation Model (DEM) (Farr et al., 2007);
- soil properties, derived from SoilGrids, at about 250 m × 250 m resolution (Hengl et al., 2017);
- ground motion properties, derived at about 1 km × 1 km resolution from the U.S. Geological Survey (USGS) ShakeMap system (Worden and Wald, 2016).

Overall, we initially select 19 covariates, here listed in Table 1. From the SRTM DEM, we obtained nine covariates representing terrain morphometric properties known to be related to the presence or absence of landslides, and specifically EQILs. We computed the Terrain Slope, because steepness is known to balance the retaining and the destabilising forces (Taylor, 1948). Planar and Profile Curvatures influence convergence and divergence of shallow gravitational processes and

Table 1
Summary of our initial covariate set.

Covariate	Acronym	Reference	Unit
Terrain Slope	*Slope*	Zevenbergen and Thorne (1987)	deg
Planar Curvature	*PLC*	Heerdegen and Beran (1982)	1/m
Profile Curvature	*PRC*	Heerdegen and Beran (1982)	1/m
Vector Ruggedness Measure	*VRM*	Sappington et al. (2007)	unitless
Topographic Wetness Index	*TWI*	Beven and Kirkby (1979)	unitless
Terrain Relief Intensity	*Relief Int*	Jasiewicz and Stepinski (2013)	m
Terrain Relief Range	*Relief Range*	Jasiewicz and Stepinski (2013)	m
Terrain Relief Variance	*Relief Var*	Jasiewicz and Stepinski (2013)	m
Distance to Stream	*D . stream*	*e.g.*, Samia et al. (2020)	m
Landform Classification	*LC*	MacMillan and Shary (2009)	unitless
Slope Unit Area	A_{SU}	Lombardo et al. (2020b)	m^2
Slope Unit Maximum Distance	D_{SU}	Castro Camilo et al. (2017)	m
Slope Unit Elongation Index 1	D/A	Castro Camilo et al. (2017)	unitless
Slope Unit Elongation Index 2	$D/\sqrt{A}$	Castro Camilo et al. (2017)	unitless
Bulk Density	*BD*	Hengl et al. (2019)	$kg\ m^{-3}$
Depth to Bedrock	*DB*	Shangguan et al. (2017)	m
Clay Fraction Concentration	*CFC*	Wan and Wang (2018)	g/g × 100
Peak Ground Acceleration	*PGA*	Wald et al. (1999)	g_n
Microseismic Intensity	*MI*	Wald et al. (2012)	unitless

overland flows (Ohlmacher, 2007). The Vector Ruggedness Measure (Sappington et al., 2007) is a proxy for terrain roughness (Amatulli et al., 2018) and Topographic Wetness Index is a function of the local slope and of the upstream contributing area that quantifies the topographic control on hydrological processes (Grabs et al., 2009). We computed three possible realizations of the Terrain Relief namely intensity, range, and variance (Stepinski and Jasiewicz, 2011). These topographic representations are meant to carry the signal of gravitational potential energy across the landscape. The idea is that, taking aside the role of other predisposing factors, a location with a higher relief than another also has a higher potential energy. As a result, the same potential energy is converted into kinetic energy if a landslide occurs, hence the resulting runout should be larger than the theoretical runout of a landslide failed with a lower relief. The relief intensity is computed as the average difference between the elevation of a grid-cell and those included in a neighbourhood that we chose within a diameter of 1 km. Conversely, the relief range is expressed as the difference between the minimum and maximum elevations within the same circle. Furthermore, the relief variance expressed the variability of the elevation values within the same circle. We also calculate the distance to streams as the Euclidean distance from each 30 m × 30 m grid cell to the closest streamline. We note here that the parameterization used to extract the river network has been kept consistent across each of the 25 study areas. The last covariate we obtained from the DEM consists of Landforms (or Landform Classes). These are represented by five landforms, from L1 to L5, representing flat topographies in L1, foot slope and valley in L2, spur and hollow in L3, slope, ridge, shoulder in L4 and summit in L5. In addition to the mentioned morphometric covariates, we selected four additional covariates describing the geometric properties of our landscape partitioning into SUs, namely: the slope unit area, A_{SU}; the maximum distance between any given pairs of points within a SU, a measure of the SU elongation, D_{SU}. From these two geometrical properties, we compute two shape indices both indicating the elongation or circularity (these measures are reciprocal) of the given SU. The first of the two indices is computed as the maximum distance divided by the SU Area (D_{SU}/A_{SU}); and the second corresponds to ratio of the maximum distance divided and the root square of the SU Area ($D_{SU}/\sqrt{A_{SU}}$). Due to the global nature of our study, we initially considered also soil physico-chemical parameters derived from SoilGrids, (Hengl et al., 2017). We considered the bulk density for it expresses the weight of the soil draping over the underlying rock and thus controls the failure mechanism (Adams and Sidle, 1987; Cheng et al., 2012). Similarly, the soil depth to the bedrock expressed the thickness of material that can potentially fail, where the thicker the failed soil column the larger the landslide is expected to be (Lombardo et al., 2016; Lagomarsino et al., 2017). As for the soil clay content, this property should carry the signal of potentially swelling soils (Khaldoun et al., 2009).

Two seismically-related covariates provide spatially-distributed ground shaking characteristics for the 25 earthquakes that caused the EQILs in our study areas, namely, the microseismic intensity, *MI* (Wald et al., 2012); and the peak ground acceleration (*PGA*), expressed in units of gravity (*g*) at 1 km × 1 km resolution (PGA, Wald et al., 1999). These deterministic estimates of the ground motion represent the severity of ground shaking contributes to the destabilising forces (*e.g.*, Nowicki et al., 2014; Kritikos et al., 2015; Meunier et al., 2007).

We remind here that the properties listed above are computed for grid cells. As we opt for a different mapping unit (see Section 3.2), each property is pre-processed to aggregate the lattice information to the chosen units (see Section 3.4). Also, we chose a large set of properties to incorporate as much information as possible. Nevertheless, our modelling protocol will feature a variable selection step aimed at removing non-informative or redundant properties (see Section 4).

3.4. Pre-processing strategy

We used landslide area as our dependent (target) variable, and we measured the size of each landslide as the planimetric area of the polygon encompassing it, *i.e.*, *landslide size* = A_L. This information was then aggregated per SU and expressed on the natural logarithmic scale, *i.e.*, $\log(A_L)$. Specifically, we prepared two landslide datasets, which we used to construct two different models. For our first model (*"Max model"*), we computed the maximum area of all the landslides included in each slope unit, A_{Lmax}. For our second model (*"Sum model"*), we selected the sum of the areas of all the landslides per slope unit, A_{Lsum}.

We provide a graphical sketch of our aggregation scheme in Figure S1, and we refer to the Supplementary Material for a more detail description. For conciseness in the main text, we have extracted two metrics A_{Lmax} and A_{Lsum}, which represent the maximum landslide size per SU and the sum of all landslide sizes per SU. They will represent the prediction target of our model.

In addition to the preparatory steps for the target variable, the set of covariates we listed in Section 3.3 have also been preprocessed. For each morphometric, soil and seismic property, we computed the mean and standard deviation of all the grid cells contained in a SU. Conversely, we assigned to each slope unit the signal of the Landform class with the largest extent. We stress here that this step may smooth out the signal of less present Landform classes although they may still contribute to the failure initiation.

In Fig. 2 we show the distribution of few covariates we computed, for each of the 25 study areas. Notably, most of them are distributed differently among study sites. Therefore, to respect the unity of each site, in our modelling scheme we introduced an additional covariate expressing the given earthquake. In doing so, we assigned an earthquake ID to each slope unit. Further details on how this covariate is used in our model are provided in Section 4.

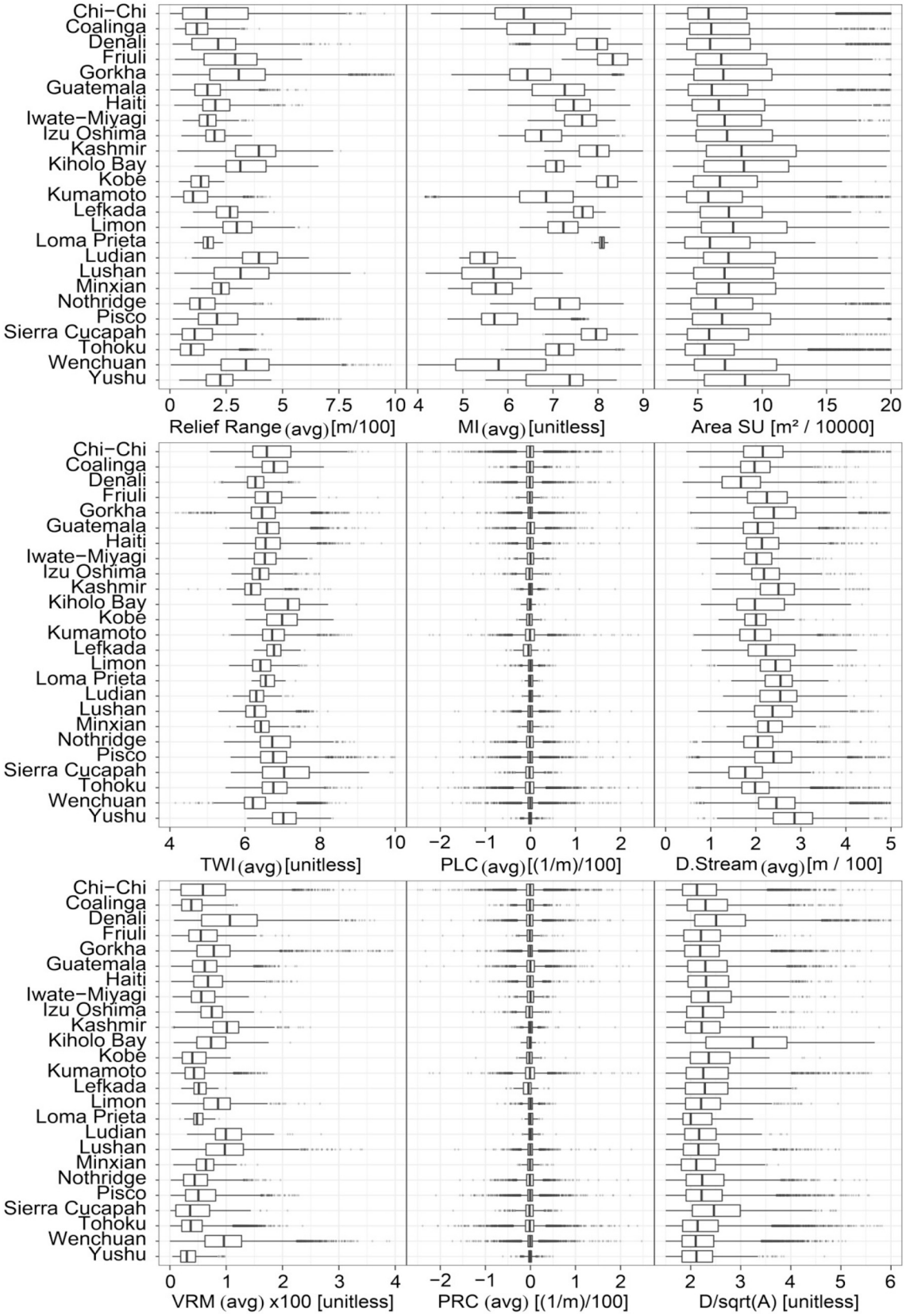

Fig. 2. Distribution summary of nine example covariates, for each of the earthquakes under consideration. Notably, the units along the abscissas have been transformed into integers for pure graphical purposes.

4. Modelling and inference

In this section, we present the statistical models assumed to be capable of fitting and predicting the spatial distribution of observed A_{Lmax} and A_{Lsum}, which will also be used to predict unobserved landslide sizes (*i.e.*, A_{Lmax} and A_{Lsum} for a SU with no landslide). Below we provide details in terms of the theoretical (Bayesian) framework, the model structure and components, as well as the computational aspects of the inference approach.

4.1. Statistical modelling

Here, we describe our modelling framework, which we adopt to understand the (possibly non-linear) effect of the explanatory variables over the landslide size. We assume that landslide sizes in the considered terrain mapping unit **s**, follow a log-Gaussian distribution with an additive structure in the mean and a site-specific variance. The mean is our main object of interest, and we would like to describe it accurately. We mathematically formalise our previous assumption as follows: let $A_L(\mathbf{s})$ be the landslide size at slope unit $s \in \mathcal{S}$, where $\mathcal{S}$ represents all the study area. $A_L(\mathbf{s})$ can be either the largest possible landslide (A_{Lmax}) or the sum of landslide sizes (A_{Lsum}) over the considered mapping unit. Then,

$$\begin{aligned} log\{A_L(s)\} &\sim \mathcal{N}(\mu(s), 1/\tau), \\ \mu(s) &= \alpha + \sum_{m=1}^{M} \beta_m x_m(s) + \sum_{l=1}^{L} f_l(z_l(s)), \end{aligned} \tag{1}$$

where:

- $\tau = 1/\sigma^2 > 0$ is the precision parameter (reciprocal of the variance) that measures the concentration of all values $\log\{A_L(\mathbf{s})\}$, $s \in \mathcal{S}$, around their mean $\mu(\mathbf{s})$. As mentioned before, our main focus is on the mean of the landslide sizes rather than their variances. Therefore, we assume a reference prior distribution for τ, which means that the prior is guaranteed to play a minimal role in the posterior distribution (Gelman et al., 2013). Specifically, we consider a vague prior by assuming that $\tau \sim \text{Gamma}(1, 5 \times 10^{-5})$ *a priori*, so that the precision is centered at 20,000 and has a huge variance of 4×10^8.
- α is a global intercept,
- the coefficients $(\beta_1, \ldots, \beta_M)^T$ quantify the fixed effects of the chosen linear covariates $\{x_1(\mathbf{s}), \ldots, x_M(\mathbf{s})\}$ on the mean response, and
- $\{f_1(\cdot), \ldots, f_L(\cdot)\}$ is a collection of functions that characterize non-linear effects defined in terms of a set of bins $\{\mathbf{z}_1, \ldots, \mathbf{z}_L\}$. These are explained below.

We adopt a Bayesian approach, and therefore assume that the model coefficients β_m and $f_l(\cdot)$, $(m = 1, \ldots, M,\ l = 1, \ldots, L)$ are unknown and random, with a joint Gaussian distribution *a priori*. This modelling approach corresponds to the class of latent Gaussian models, which includes a wide variety of commonly applied statistical models (Rue et al., 2017; Hrafnkelsson et al., 2020; Jóhannesson et al., 2021). To identify the covariates that may enter to the $\log(A_{Lmax})$ or $\log(A_{Lsum})$ models in the form of linear or non-linear predictors, we conducted a model selection. The selection was based on the Watanabe-Akaike information criterion (WAIC; Watanabe, 2010, 2013) and the Deviance information criterion (DIC; Spiegelhalter et al., 2002), which measure a model's goodness-of-fit, while penalizing its complexity, in order to favour parsimonious models and prevent overfitting. Lower values of these criteria lead to better models. For each covariate that was linearly included in the models, we tested whether a non-linear random effect for the covariate would significantly improve the model. For both response variables, the final models include the same linear and non-linear random effects. The latter ones take the form of random intercepts and random walks of order 1 (see Table 2). Random walks of order 1 (RW1) can be defined as follows: for any continuous covariate $x_l = x_l(\mathbf{s})$, let $\mathbf{z}_l = (z_{l,a}, \ldots, z_{l,K_l})^T$ be a discretisation of x_l into K_l equidistant bins. If

Table 2
Summary of (only) the selected covariates for both models. In the second column, RW1 refers to random walks of order 1, while RI refers to random intercepts.

Fixed effects	Random effects
Area SU, $D/\sqrt{A}$, Relief range (mean and sd),	RW1: Mean slope
Distance to streams (mean and sd), Sd of slope, VRM (mean and sd), PLC (mean and sd), PRC (mean and sd), TWI (mean and sd), MI (mean and sd)	RI: Landform and Earthquake inventories

we assume that the random non-linear effect $f_l(\cdot)$, defined on $\mathbf{z}_l$, satisfies

$$\Delta_{l,j} = f_l(z_{l,j}) - f_l(z_{l,j-1}) \sim \mathcal{N}(0, 1/\kappa_l),$$

then $f_l(\cdot)$ is a normal random walk of order 1 with precision parameter $\kappa_l > 0$, which controls the "smoothness" of the random walk. Note that since $f_l(z_{l,j}) = f_l(z_{l,j-1}) + \Delta_{l,j}$, at each covariate level j, then $f_l(z_{l,j})$ is obtained as a displacement of random length and direction from the previous value $f_l(z_{l,j-1})$. The dependence induced by this type of construction is particularly useful when few values of the original covariate x_l are contained in a particular bin.

Random intercept or independent and identically distributed Gaussian random effect models (iid models) are one of the simplest ways to account for unstructured variability in the data. For every slope unit $s \in \mathcal{S}$, the precision matrix of iid random effects is $\gamma(s) \times \mathbb{I}$ where $\mathbb{I}$ denotes the identity matrix and $\gamma(\mathbf{s}) \sim \text{Gamma}(1, 10^{-5})$ *a priori*. As shown in Table 2, we used iid models for Landform and Earthquake inventory.

4.2. Uncertainty quantification and the bootstrap

The modelling approach presented above describes landslide sizes through a set of covariates at each specific slope unit, without taking into account possible spatial dependence between slope units in the same event. A proper spatial model should include interactions between slope units, which in statistical terms implies defining a covariance structure for all the 22,343 non-missing slope units. Although it is possible to define such structures using a neighbouring approach where only close-by slope units will interact, and therefore the associated covariance matrix might be less dense, the high-dimensionality of our data prohibits us from fitting such a model. Alternatively, we could have separate models for each of the 25 inventories and define the covariance structure locally. However, model comparison would be challenging, as not all covariates might have the same effect over all the events.

In terms of statistical estimation, not addressing the spatial dependence between slope units mainly affects the uncertainty of the estimates, *i.e.*, the credible intervals. Pointwise estimates remain mostly unchanged. To assess the uncertainty of parameter estimates, we here use a parametric bootstrap procedure accounting for spatial dependence in the model residuals. The Bootstrap is a resampling method that can be used to assign measures of accuracy to estimates. Our parametric Bootstrap is constructed as follows: for any of the two models, we compute the model residuals (*i.e.*, we subtract to the observed values the fitted values, $log(A_L)(s) - \widehat{\mu}(s)$). Then, we fit a spatial model to the residuals of each inventory separately (*i.e.*, treating inventories as independent). We then generate 300 residual Bootstrap samples using the fitted spatial model. To express these samples in the scale of the data, we add back the fitted values $\widehat{\mu}(s)$, given rise to 300 Bootstrap samples of landslide sizes. Finally, we fit the model in (1) to each one of these samples, for both models. The spatial model fitted to the residuals corresponds to a stationary isotropic Gaussian process with an exponential covariance function (see, *e.g.*, Cressie, 2015, Section 2.3). The Bootstrap is essential for accurate quantification of the uncertainty, as, without it, uncertainty estimates might be too optimistic, *i.e.*, parameter credible intervals might be too narrow in both models.

4.3. Bayesian inference with R-INLA

Bayesian inference is typically performed using computationally expensive approaches such as Markov chain Monte Carlo (MCMC). Here, we overcome these computational costs using the integrated nested Laplace approximation (INLA; Rue et al., 2009). When exploiting INLA, the posterior distribution of the parameters of interest are approximated using numerical methods, which makes it possible to compute the required quantities in a reasonable amount of time. The INLA methodology is conveniently implemented in the R-INLA package (Bivand and Piras, 2015) and we use it to obtain an accurate approximation of posterior marginal densities of interest, such as those for $\mu(\mathbf{s})$ and the parameters introduced in Section 4.1.

4.4. Landslide area simulation

The R-INLA package offers built-in functions to compute posterior samples even at locations where we do not have observations. In other words, using the model fitted to the complete dataset, we can infer the distribution of each missing landslide size. Internally, R-INLA treats missing values as values that we need to predict. Therefore, if we provide the set of explanatory variables accompanying the missing landslide areas, R-INLA will use the fitted model to predict (or fill in) the missing values. In practice, R-INLA performs model fitting and prediction at the same time, producing all the required results in a short amount of time. Here, we generated 5000 posterior samples for each missing landslide area. These posterior distributions are summarized in term of their mean and 95% credible intervals.

To put it simply, in a Bayesian framework, the estimation of the posterior regression coefficients consists of a distribution of possible values. Therefore, by sampling at random each distribution for the effect of each covariate, it is possible to statistically simulate a given process. Here, we simulated 5000 predictive functions to estimate the mean behaviour as well as the uncertainty in the landslide area prediction for each SU. This is a crucial step because those SUs encompassing one or more landslides provide enough information to assess the whole spectrum of possible landslide areas (mean and 95% CI for both the Max and Sum models). However, the SUs where no landslides have been recorded require the simulation step to recover analogous information.

4.5. Goodness-of-fit and predictive performance assessment

We here describe numerical and graphical methods to assess the goodness-of-fit and the predictive performance of our models.

- **Probability integral transform (PIT):** PIT values are useful leave-one-out goodness-of-fit measures. They are computed as follows

$$P_i = F_{-i}(y_i), \quad i \in \{1, \ldots, |\mathcal{S}|\},$$

where F_{-i} is the cumulative distribution of the i-th observation, y_i, obtained from a model fitted using all the available data except y_i, $\mathcal{S}$ contains all the slope units $\mathbf{s}$, and $|\mathcal{S}|$ is the cardinality of $\mathcal{S}$, *i.e.*, the number of slope units. A model with a perfect predictive ability should have PIT values closely distributed according to a standard uniform distribution. Indeed, assuming that F_{-i} is continuous (which is the case here) the distribution of P_i, $i = 1, \ldots, |\mathcal{S}|$, can be written as

$$Pr(P_i \leq u) = Pr(F_{-i}(y_i) \leq u) = Pr(y_i \leq F_{-i}^{-1}(u)), \quad u \in (0, 1).$$

The model F_{-i} has a perfect prediction ability if it is able to generate y_i (the value that was left out). This means that F_{-i} is a perfect prediction if $y_i \sim F_{-i}$ which, in turns, implies that

$$Pr(y_i \leq F_{-i}^{-1}(u)) = F_{-i}(F_{-i}^{-1}(u))) = u.$$

The above equation implies that the distribution of the PIT values $\{P_1, \ldots, P_{|\mathcal{S}|}\}$ should be uniformly distributed in (0, 1). The uniformity of the PIT values is a necessary condition for the prediction to be perfect (Gneiting et al., 2007) and any deviation from uniformity, implies a decrease in performance.

- **Plot of observed vs. fitted values:** In such a plot, we can see how much the fitted values deviate from the actual observed landslide areas. A model with a reasonable performance should produce values aligned with the main diagonal (*i.e.*, the 45° line).
- **Probability coverage:** given a probability $\alpha \in (0, 1)$, we compute the proportion of times that a $(1-\alpha)100$ % credible interval contains the observed data. If the underlying model is adequate, then the computed proportion (usually called sample coverage) should be close to $(1-\alpha)100$ % (the nominal coverage). In practice, the Bayesian methodology allows us to simulate from the posterior distribution in order to compute as many credible intervals as desired.

  For a readership who is unacquainted with the coverage concept, below we provide a brief and simple explanation. Using posterior simulations, we construct 5000 estimates for each observed A_L value. Then, for each A_L, we compute sample p-quantiles, with $p = \{0.025, 0.05, 0.075, \ldots, 0.950, 0.975\}$ (a sequence from 0.025 to 0.975 with steps of size 0.025). These sample quantiles allow us to construct credible intervals of sizes $(1-\alpha)100\,\% = \{10\,\%, 15\,\% \ldots, 90\,\%, 95\,\%\}$. Then, we count how many times the observed A_L values fell within these intervals. If the model is adequate, for a credible interval of size $(1-\alpha)100$ % the number of times the observed A_L is contained should be close to $(1-\alpha)100$ %. For instance, a 95% credible interval should contain 95% of the observed A_L values. Therefore, if we plot the nominal coverage vs. the sample one, a reasonable model will show points aligned with the 45° line.

5. Results

In this section we present a summary of the model performance for each landslide size models, $\log(A_{Lmax})$ and $\log(A_{Lsum})$. We then provide an overview of the inferred covariate effects and conclude presenting a graphical translation of the model's output into map form.

5.1. Predictive performance

Fig. 3 shows an overview of the model performance presented in agreement with the three metrics we explored, namely, probability integral transform (PIT) plots, observed vs. fitted values and coverage probabilities. The top row shows the performance of the Max model, while the bottom row shows the performance of the Sum model. The collection of probabilities detailed in Section 4.5, computed using all the training data, gives rise to the histogram in Fig. 3a,d. We can see that both models capture the bulk of the distribution (bars close to the dashed line) reasonably well, but they do not seem to appropriately capture the tails of the landslide size distribution (bars far from the dashed line). The latter is expected since the normal and log-normal distributions have light tails, which implies that the model will give fairly low probabilities (*i.e.*, very close to 0) to extreme landslide sizes. We recall here that for a model to be optimal, the PIT plot should exhibit a uniform distribution. Here, we can see some moderate departure from the uniform distribution in both cases, but this is expected for such a large dataset combining various heterogeneous EQIL inventories.

Overall, the Max model seems to be better calibrated than the Sum model. Observed vs. fitted values look similar for both models (Fig. 3b, e), although the Max model exhibits pair of points slightly better aligned and equally spread along the 45° line. As for the coverage probabilities (Fig. 3c,f), both models appear to be surprisingly excellent with most of the nominal to sample coverage pairs very well aligned with the 45° line and the bulk of the distribution showing a negligible deviation from it.

As mentioned in Section 4.5, the coverage plots are computed by simulating 5000 samples from each model and counting the proportion

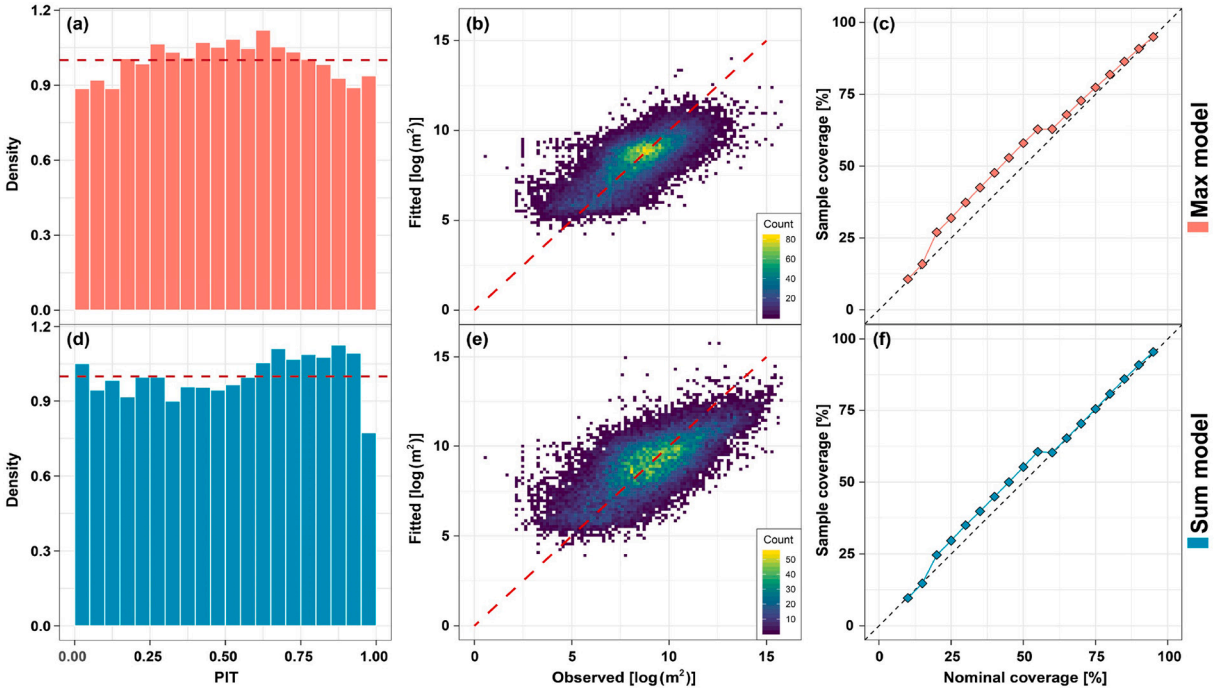

Fig. 3. Left to right: Probability integral transform (PIT) plots, fitted vs. observed plots (in log-scale), and coverage probabilities for the Max (top) and Sum (bottom) models.

of times the observed data are within a $(1-\alpha)100$ % simulated-based credible interval, with $\alpha = \{0.05, 0.10, \ldots, 0.90\}$ (the nominal coverage). A model with a reasonable coverage should give a proportion close to $(1-\alpha)100$ %. We can see that our models succeed in recovering the nominal coverage for extreme nominal coverage values, but they are a bit off for central nominal coverage values. Overall, the Sum model performs slightly better than the Max model.

5.2. Linear covariate effects

Fig. 4 shows the estimated coefficients of linear (or fixed) effects (except for the intercept) for the Max and Sum models. Notably, we plot the 95% credible intervals originated from the Bootstrap rather than directly from INLA, which incorrectly assumes conditional independence for model fitting. We recall here that because of this, INLA may largely underestimate the uncertainty compared to Bootstrap, which more realistically accounts for spatial dependence at the data level. In light of this, here we only report the Bootstrap uncertainty and do not show the uncertainty directly estimated with INLA.

The selected covariates, that have been rescaled to have mean 0 and variance 1, show relatively strong positive and negative influences on landslide sizes. More specifically, out of 17 covariates used linearly only 7 appeared to be significant for the Max model, and 8 for the Sum model. Non-significance does not necessarily imply that the model is not influenced by these covariates. Significance indicates that the model is 95% certain of the role (either positive or negative) of the given covariate with respect to the landslide size. Moreover, the extent to which a covariate—significant or not—contributes to the model is summarized by the absolute value of the posterior mean regression coefficient.

In this sense, the largest linear contributors for the Max model are *MI (avg)* and *Relief rng (avg)*, both with an absolute mean regression coefficient of 0.50. Besides, *Slope (std)*, *VRM (avg)*, *PRC (std)* and Area SU contribute with absolute posterior mean coefficients of 0.42, 0.18, 0.16 and 0.13, respectively. From these ranks, the contribution becomes less prominent and it decays down to the least contributor represented by *MI (std)* with $|\widehat{\beta}| = 0.0007$. The covariates appeared to be ranked with a primary control on the estimated landslide size exerted by the relief, a proxy for gravitational potential energy and by the MI, a proxy for the ground motion stress. Intuitively, the easiest interpretation of the relief, is that from a SU with a larger relief or gravitational energy, one should expect larger landslides. However, this type of interpretation is difficult to be uniquely identified because the inventories mix up landslides of different types without a distinction between failure and runout zones. The role of the slope steepness is also well represented in the model as well as the dimension of the mapping unit itself. Specifically, these

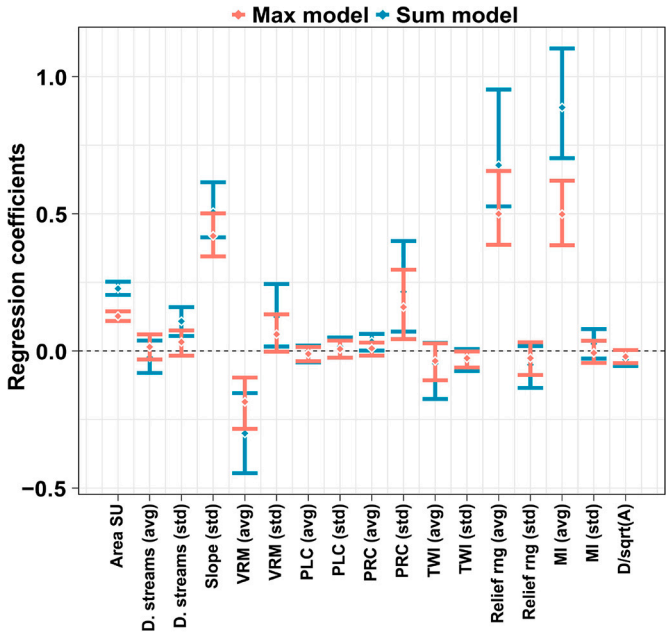

Fig. 4. Posterior means (dots) of fixed linear effects (except the intercept) with Bootstrap-based 95% credible intervals (vertical segments) for the Max and Sum models. The horizontal black dashed line indicates no contribution to the landslide sizes.

covariates present a significant and positive posterior distribution which contributes to increase the expected landslide size (*e.g.*, Medwedeff et al., 2020; Valagussa et al., 2019). Conversely, a negative regression coefficient, *e.g.*, for *VRM (avg)*, implies that larger landslide sizes for the Max model are expected for smaller *VRM (avg)* values. The negative contribution of the *VRM (avg)* is also consistent with the current literature. For instance, Frattini and Crosta (2013) suggested that high roughness implies a more dissected landscape with smaller sub-sectors across a given slope unit. Thus, this setting could act as a limiting factor for landslide size.

For the Sum model, the dominant fixed effect appears to be the *MI (avg)*, with an absolute mean regression coefficient of 0.89. This is followed by *Relief rng (avg)* with $|\widehat{\beta}| = 0.68$, *Slope (std)* with $|\widehat{\beta}| = 0.51$, *VRM (avg)* with $|\widehat{\beta}| = 0.30$, *Area SU* with $|\widehat{\beta}| = 0.23$, *Prof Cur (std)* with $|\widehat{\beta}| = 0.22$ and *VRM (std)* with $|\widehat{\beta}| = 0.12$.

5.3. Non-linear covariate effects

Fig. 5 displays all the non-linear (or random) covariates' effects featured in our model, by plotting the estimated coefficients in terms of posterior mean and Bootstrap-based 95% credible intervals. Two panels (top row and bottom left) report covariates that have been used in a purely categorical form, *i.e.*, with class effects being mutually independent *a priori*. The remaining panel (bottom right) shows the covariate *Slope (avg)* being used as an ordinal variable with an adjacent inter-class dependency driven by a random walk (see Section 4.1).

The *Earthquake Inventories* multiple intercepts (Fig. 5a) show a complex and varying behavior. To interpret this panel, the regression constants are site-specific indices of differences in landslide area response to the ground motion. In other words, with respect to the mean landslide area across the whole dataset we used, the values reported here lead to variations in landslide size typical of specific landscapes. For instance, at a preliminary visual examination, the Gorkha earthquake clearly stands out with the smallest mean regression constant out of the 25 cases; the largest posterior mean is associated to the Guatemala earthquake. Finally, few earthquakes inventories are aligned along the zero line. In other words, they display no positive nor negative anomaly with respect to the average landslide size of all 25 cases combined. More details and an extensive interpretation of these results will be provided in Section 6.

A much simpler situation prevails for the Landforms (Fig. 5b). In fact, no landform class appears to be significant in our case and they all lay along the zero line, indicating a negligible effect onto the final model. We will discuss this in Section 6.

The *Slope (avg)* panel (Fig. 5c) shows a clear nonlinear behavior both in the Max and Sum models. SUs with an average steepness up to approximately 25 degrees do not contribute to vary the estimated landslide size. From this threshold to larger steepness values, the Max model shows a mild increase in the *Slope (avg)* regression coefficients, whereas the Sum model also increases but with a much steeper trend.

5.4. Landslide area classification

We opt to translate the model results in map form following two

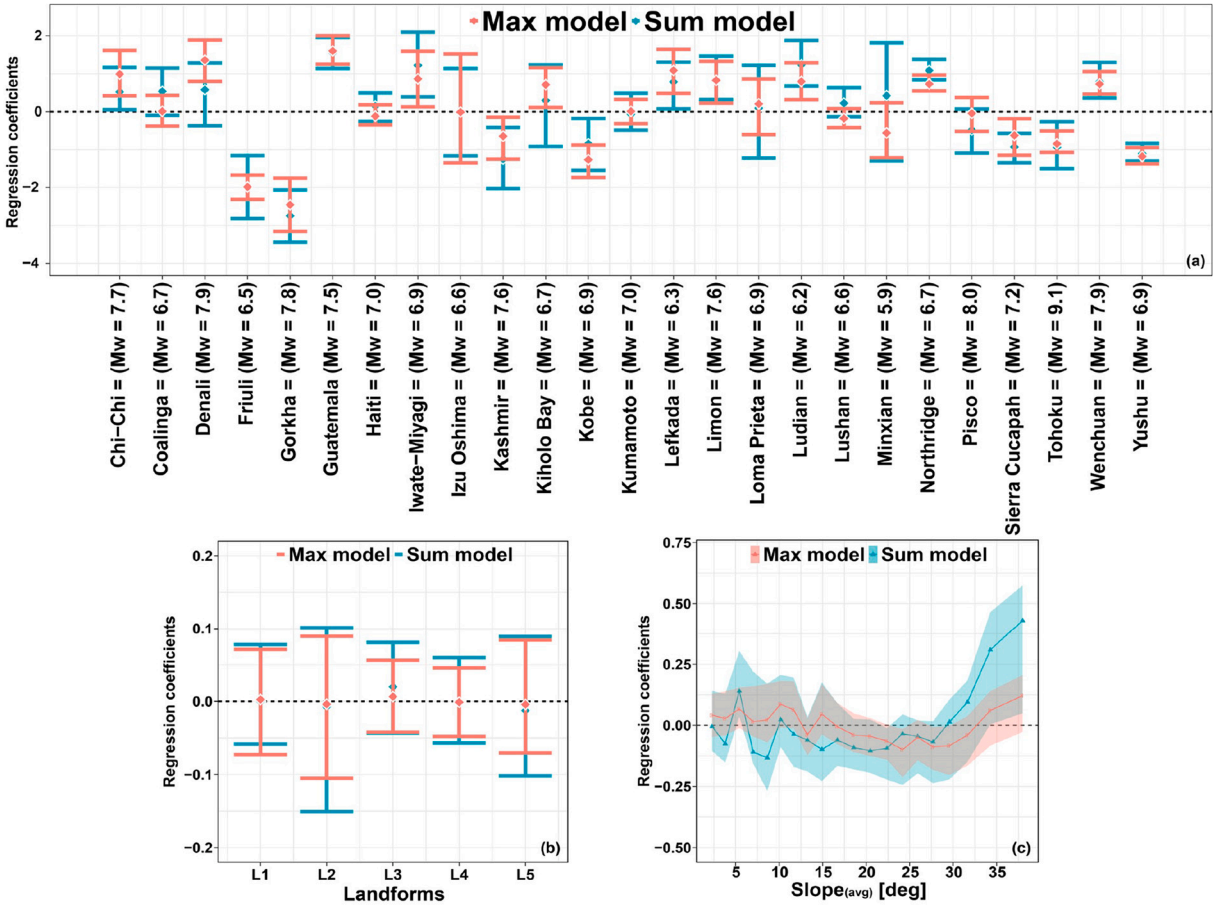

Fig. 5. Random effects for the Max and Sum models: earthquake inventories (top), landform classes (bottom left), and *mean slope* (Slp, bottom right). For the earthquake inventories and landform classes, the dots show the posterior mean, while the segments correspond to the Bootstrap-based 95% credible intervals. For *mean slope*, the curves show the posterior mean, while the shadowed polygons correspond to the Boostrap-based 95% credible intervals. In all the plots, the black horizontal dashed line indicates zero (*i.e.*, no contribution to the landslide sizes).

approaches. The first one is simply to display the $\log(A_L)$ observations and estimates in their original continuous scale. The second approach introduces a classification step in our mapping procedure which is graphically summarized in Fig. 6. Specifically, we start by computing the best fit line in a two-dimensional space defined between observed and predicted landslide areas. From the observed cases we compute four quantiles at specific intervals ($\tau = 0.05$, 0.25, 0.75 and 0.95). The observed landslide area (be it Max or Sum) values associated with each of the quantiles are then projected to the predicted landslide areas by intersecting the best fit line. As a result we are able to also show a common classification scheme for Very Small (VS), Small (S), Medium (M), Large (L) and Very Large (VL).

It is important to note that there were several options. For instance, any GIS environment generally offers the option to visualize spatial data by cutting off values above and below a certain standard deviation. This could have helped us to improve the visual agreement between observed and predicted landslide sizes. In fact, our model tends to be "too smooth" (as expected with Bayesian regression models), in the sense that it overestimates the left tail of the $\log(A_L)$'s distribution and underestimates its right tail. However, we chose to keep the data intact to highlight strengths and weaknesses. The opposite situation could have taken place if we would have classified according to two separate boxplots, one for each axis. This would have maximized the differences driven by the log-Gaussian approximation. Therefore, we chose an intermediate option which we believe to be fair and representative enough of the model performance converted into map form.

5.5. Landslide size predictive mapping

In this section we geographically translate and report the outcome of our modelling framework. However, because we modelled 25 EQIL inventories, showing each corresponding figure would have overly lengthened the manuscript. Therefore, we chose to provide two examples where our Max and Sum models performed well (Haiti and Wenchuan) and two examples where we find a poor agreement between observed and predicted Max and Sum landslide sizes (Gorkha and Chi-Chi). The remaining 23 cases are separately provided in the Supplementary Material for clarity, both for the Max and Sum models.

Each of the four figures introduced above contains the following information:

1. Observed landslide area map using continuous values.
2. Predicted landslide area map using continuous values.
3. Observed landslide area map using the classification explained in Section 5.4.
4. Predicted landslide area map using the classification explained in Section 5.4.
5. 95% credible interval measured by subtracting the SU-wise 97.5 and the 2.5 percentiles obtained with INLA (see Section 4.4).
6. 95% credible interval measured by subtracting the SU-wise 97.5 and the 2.5 percentiles obtained via Bootstrap (see Section 4.2).

In summary, Figs. 7 and 8 show our proposed mapping procedure for Haiti, for Max and Sum models, respectively. In both cases, panels *a* and *b* show a strong agreement overall, with the exception of the NW sector where predicted landslide sizes are underestimated with respect to the observed counterpart. Our classification (panels *c* and *d*) produces a better match between the two maps. Furthermore, the uncertainty around the prediction (panels *e* and *f*), which is realistically higher in the bootstrap case, is relatively low with the exception of a few number of large SUs.

Similarly, Figs. 9 and 10 correspond to the Wenchuan case. The pattern of the predicted landslide sizes (both for Max and Sum models) is extremely close to the pattern shown for the corresponding observed cases, this being valid both on the continuous scale (panels *a* and *b*) and in the classified maps. This is a quite remarkable agreement between observed and predicted cases although the latter tends to slightly overestimate the former. Both for Max and Sum models, the 95% credible intervals show quite reasonable bootstrapped values both in spatial distribution and amplitude with respect to the original scale.

Figs. 11 and 12 display the estimated landslide size over space for Chi-Chi. The island of Taiwan has a rough topography, thus the prediction covers the whole island showing a reasonable pattern both for the Max and Sum models. However, the comparison between the classified landslide sizes shows a situation where the model tends to slightly overestimate the original size class. Notably, this is much more evident for the Max model rather than its Sum counterpart. The estimation is generally larger by one class or, in other words, where the original data shows medium landslide extents the model predict a large counterpart and where the observed landslide is large our model assigns a very large landslide class. This relatively low performance is reflected in the bootstrapped uncertainty levels where the size of the 95% credible interval is generally larger than the corresponding observed landslide size.

The worst case among the 25 we examined corresponds to the Gorkha earthquake (see Figs. 13 and 14). Here the Max and Sum models produce different performances where the Max one tends to generally underestimate the observed landslide size. As for the Sum model, here the bulk of the observed landslide size distribution is well represented, although the left tail is overestimated and the right tail is underestimated. Therefore, the general spatial pattern is similar between observed and predicted cases, with an upward or downward shift in the predicted classes due to under/overestimation issues. Here the Bootstrap uncertainty range is again relatively high with slightly higher 95% credible interval compared to the corresponding observed landslide size.

A deeper interpretation is provided in Section 6.

6. Discussion

This section is meant to provide the reader with an interpretation of the modelling protocol we present as well as to share our views on its limitations and strengths. The following sections will focus on one element at a time and will be concluded with our future plans for further extensions.

6.1. Performance overview

Our Log-Gaussian model of planimetric landslide areas is a global model, thus it may perform differently for each of the considered earthquakes. And yet, both Max and Sum models are generally able to characterize the $\log(A_L)$ distributions in each of the 25 study sites. We summarized this information in Fig. 15.

We recall here that the performance of both Max and Sum models appears to be quite satisfactory also when this information is graphically shown for the whole landslide size dataset (see also Figs. 3 and 6) or geographically shown for specific sites (see figures from 7–14). These predictive maps visually and intuitively demonstrate how the observed and predicted $\log(A_L)$'s patterns match. To provide a numerical overview of the models' performance for each of the 25 earthquakes, in Fig. 16 we also show the agreement among observed and predicted landslide sizes, after we performed the classification explained in Section 5.4. In this figure, we show that despite the Max and Sum models generally agree, the classified landslide size per earthquakes may be misrepresented. This is the case of Coalinga, Minxian and Yushu, both for Max and Sum models. These specific events show the least agreement among classes with a perfect match between observed and predicted being confined below 30%. Besides, the slight under- or over-estimation demonstrated by a single shift in class is larger than 50% and the large under- or over-estimation demonstrated by a two (or more) class shift characterizes 20% of the predicted landslide size.

These three cases clearly represent the worst prediction our Max and Sum models produced. Similarly, we highlight three earthquakes for which our models perform very well. This is the case for Loma Prieta,

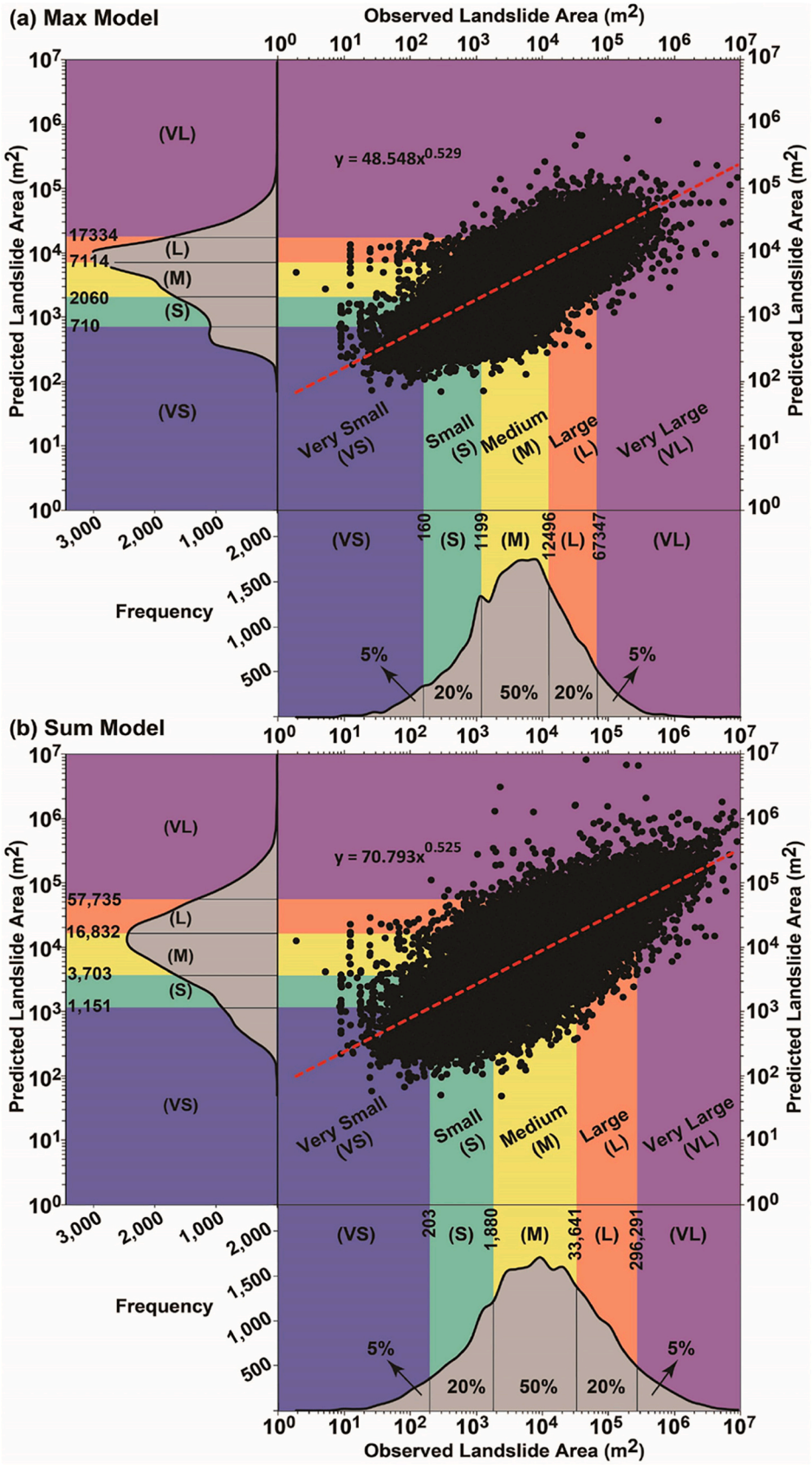

Fig. 6. Observed vs. predicted landslide areas shown together with the classification scheme implemented to create a suitable colorbar for mapping. The density plots show the common classification for Observed vs. predicted landslide areas. (For interpretation of the references to color in this figure legend, the reader is referred to the web version of this article.)

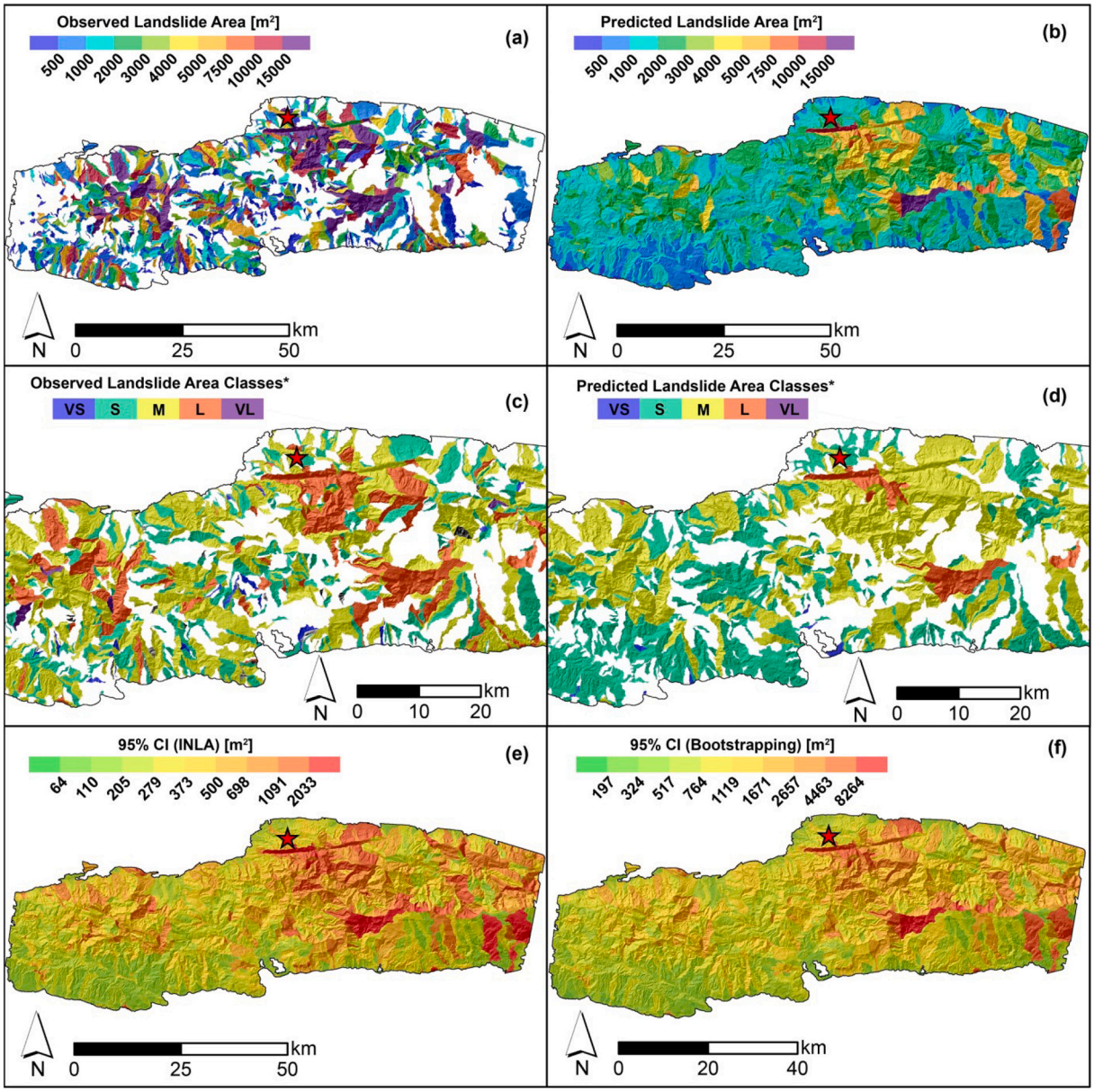

Fig. 7. Excellent agreement example for Haiti Max maps: (a) Observed maximum landslide area per SU. (b) Predicted maximum landslide area per SU. (c) Classified observed maximum landslide area per SU. (d) Classified predicted maximum landslide area per SU. (d) 95% credible interval estimated with INLA. (e) 95% credible interval estimated via bootstrap.

Limon and Izu Oshima where the two (or more) class shift characterizes less than 1% of the prediction, the one class shift corresponds to less than 45% and the perfect match is found in more than 55% of the SUs.

This overview provides a better summary of the models we propose. It certainly suggests that our models are quite performing but also that some improvements could still be achieved, possibly improving the quality of the data, the scale at which the models are built and the model structure. Each of these elements will be discussed in the following sections.

6.2. Interpretation of the covariates' role

For a model to be operational, good performances are not the only requirement. Each model component should be interpretable and make sense from a geomorphological standpoint. Here we examine how reasonable our Max and Sum models are on the basis of the estimated regression coefficients' distribution.

As briefly anticipated in Section 5.2, the fixed effects appear to be geomorphologically sound, with the exception of the *VRM (avg)*. Both for the Max and Sum models, the mean Macroseismic Intensity (MI) per SU is the largest contributor (in the Sum model case, it has a much larger posterior mean value). This may indicate that the ground motion not only plays an important role in explaining any landslide size but it may imply the *MI (avg)* is even more crucial to estimate very large aggregated landslide sizes per SU, which are part of the Sum model rather than the Max model. Similar considerations can be found in, *e.g.*, Keefer and Manson (1998) and Massey et al. (2018), where the authors mentioned a similar relation by assuming that the intensity of the ground motion decreases as a function of the distance to the rupture zone. Similarly, the *Relief rng (avg)* appears to be the second largest contributor both for the Max and Sum models. More specifically, its effect onto the landslide size estimates is equivalent to the *MI (avg)* for the Max model case and it is 24% smaller than the contribution of the *MI (avg)* in the Sum model case. This can be interpreted in terms of topographic control on

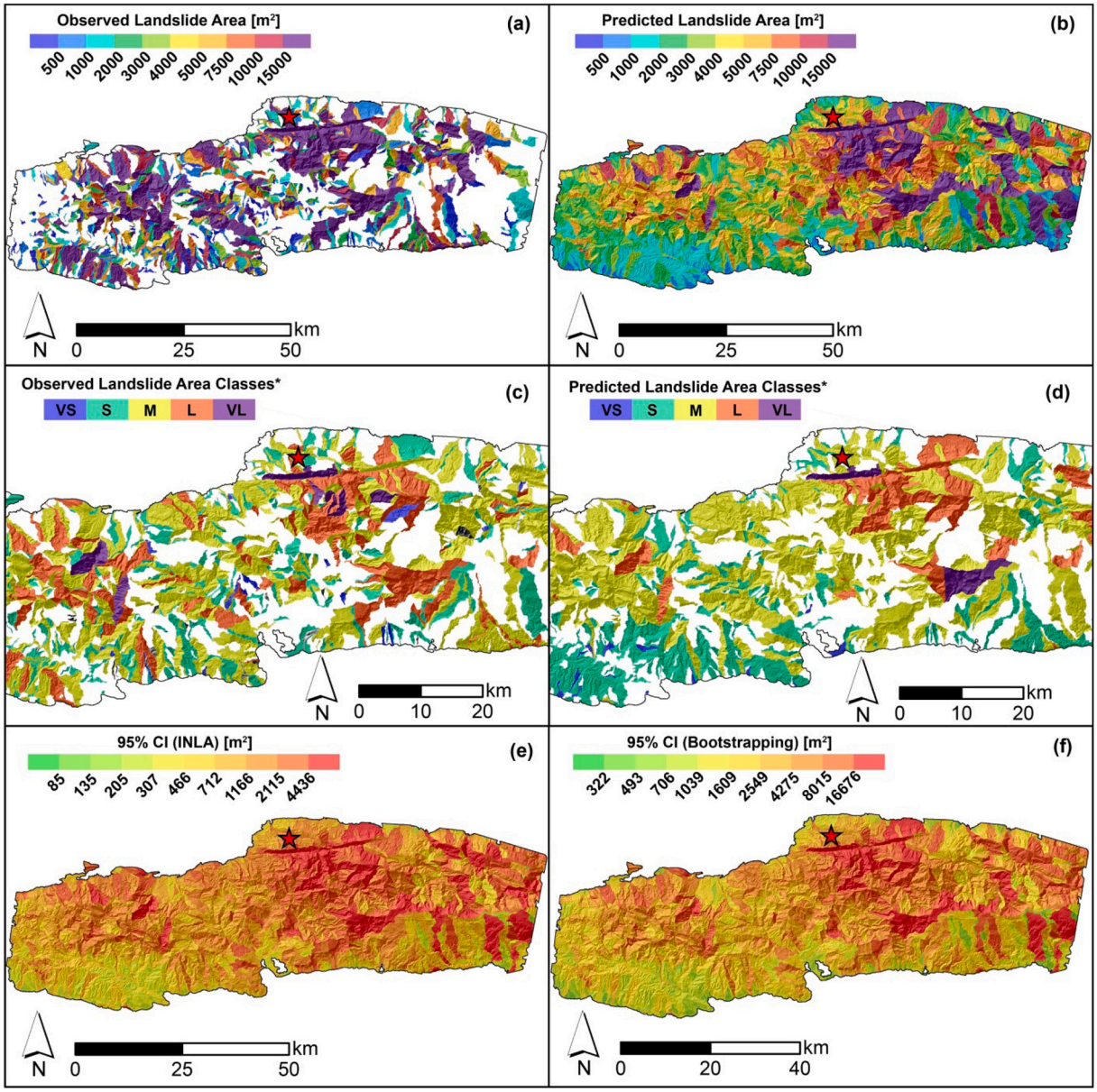

Fig. 8. Excellent agreement example for Haiti Sum maps: (a) Observed summed landslide area per SU. (b) Predicted mean of summed landslide area per SU. (c) Classified observed sum of landslide area per SU. (d) Classified predicted mean of summed landslide area per SU. (d) 95% credible interval estimated with INLA. (e) 95% credible interval estimated via bootstrap.

landslide sizes. For the Max model, the potential gravitational energy expressed by the relief is able to explain the landslide size as much as the trigger itself (*MI (avg)*). In the Sum model, although the relief is still fundamental to estimate A_{Lsum}, its contribution is ranked second overall, likely because extremely large landslide sizes do require an exceptional seismic stress to be triggered. High relief may be interpreted as a sign of relatively strong rock mass properties constituting the hillslope materials (Schmidt and Montgomery, 1995; Townsend et al., 2020) and yet the positive contribution can be linked to the higher potential gravitational energy and longer runout associated with hillslopes with high relief. Similar considerations can be found in Medwedeff et al. (2020) where the authors emphasize how much hillslope relief is crucial to control landslide sizes.

Another reassuring covariate contribution can be seen for the *Slope (std)*, both for the Max and Sum models. The variation of the steepness inside a given SU can be intuitively interpreted as a proxy for topographic roughness. For instance, if the mean steepness per SU is 40 degrees but the standard deviation is close to zero, then the whole slope unit would certainly be steep but its surface would be smooth. Conversely, in the case where the mean steepness per SU is 40 degrees but the standard deviation is 20 degrees, then one should expect the SU surface to be rough and likely hummocky at times. Such a surface should offer a bumpy landscape upon which the ground motion can act to mobilize unstable material. As a result, a significant and positive coefficient estimated for *Slope (std)* appears to be reasonable for the larger the roughness, the more available potentially unstable material should be, hence the larger the resulting landslide. *Slope (std)* also appears as a positively contributing variable in studies assessing the susceptibility of rainfall- and earthquake-induced landslides (*e.g.*, Guzzetti et al., 2005; Tanyaş et al., 2019a).

The fourth ranked covariate is more problematic. The *VRM (avg)* is an expression of topographic roughness. Therefore, one should expect a positive sign of the regression coefficient distribution, both for the Max and Sum models. However, the coefficient of *VRM (avg)* appears to be

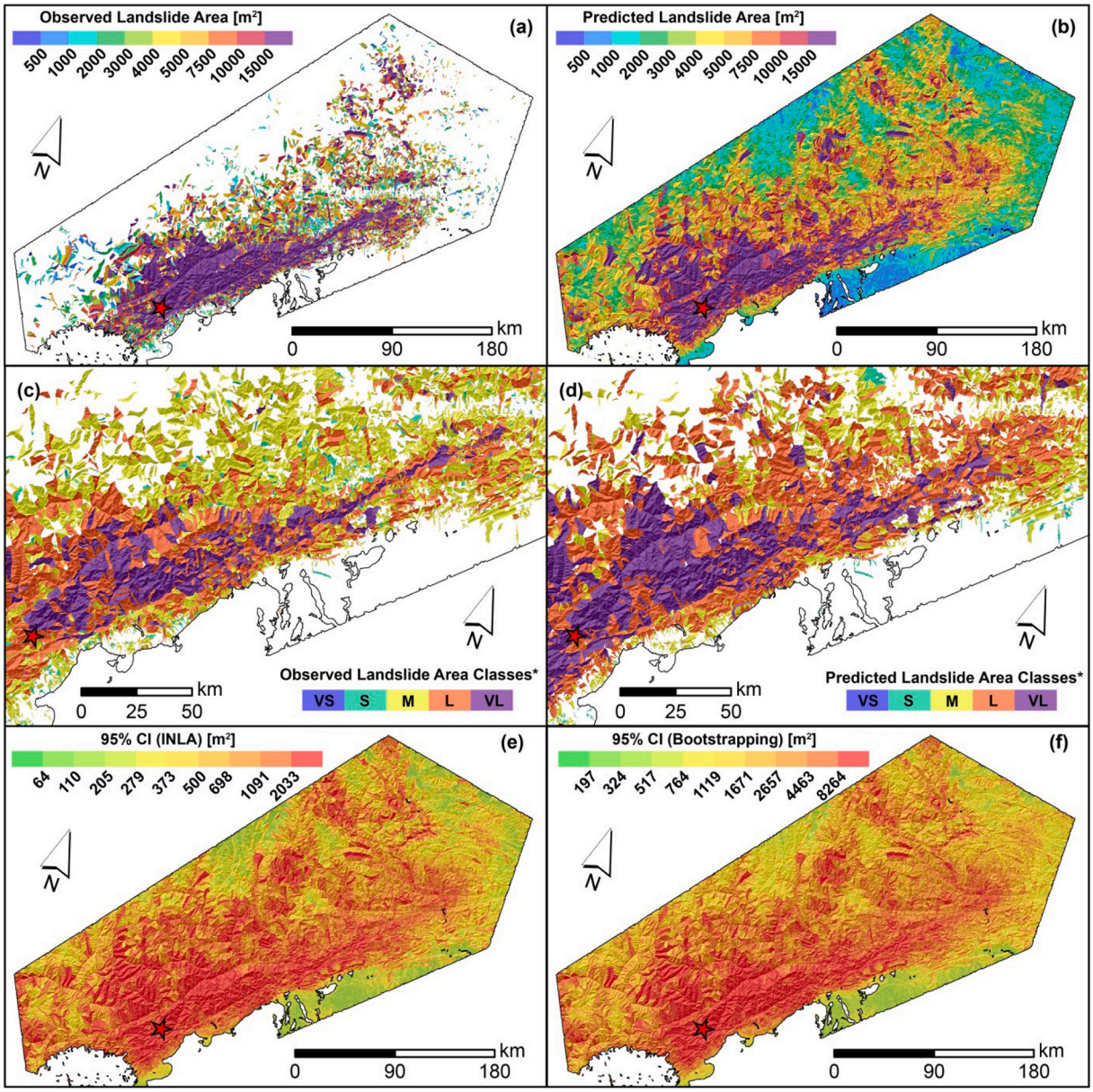

Fig. 9. Excellent agreement example for Wenchuan Max maps: (a) Observed maximum landslide area per SU. (b) Predicted maximum landslide area per SU. (c) Classified observed maximum landslide area per SU. (d) Classified predicted maximum landslide area per SU. (d) 95% credible interval estimated with INLA. (e) 95% credible interval estimated via bootstrap.

significant and negative overall, making any interpretation difficult to formulate. We believe this to be a case of a confounding covariate. In fact, although our variable selection step (see Section 4.1) included the *VRM (avg)*, this covariate still interacts with the others. Therefore, in case this covariate would share a similar signal to another one or more than one, its sign and amplitude of the regression coefficient will be influenced by other interactions. In the specific case, we believe *VRM (avg)* to be potentially interacting with more than one covariate that carries the topographic roughness information. For instance, not only the *Slope (std)* may play a similar role but also the two curvatures. In fact, the planar and profile curvatures are by definition summarizing how rough the given landscape is in two main directions. This is particularly exacerbated in case of a SU partition where we compute the mean and standard deviation for each morphometric property. In this sense, computing the standard deviation of the curvatures inside a given SU certainly stresses how rough the mapping unit is. Therefore, it can share a similar role with the *VRM (avg)*, which is estimated to be negative overall, to counterbalance different positive contributions for proxies of topographic roughness. To expand on this, both Max and Sum models estimate the *Prof Cur (std)* to be significant and positive.

As for the interpretation of the random effects (see Section 5.3 and Fig. 5a), the multiple intercept per earthquake provides an interesting point of discussion. In the Max model built for Coalinga, Izu Oshima, Kumamoto, Loma Prieta and Pisco, the intercepts appear to be non-significant. In these cases, not being significant has a particular meaning because it indicates specific earthquakes for which the model does not strictly require a regression constant. In other words, these five study sites behave in line with the average Max landslide size computed for the whole 25 datasets combined. A similar situation can be seen for the Sum model where four earthquakes (Izu Oshima, Kiholo Bay, Kumamoto and Loma Prieta) have been estimated with a non-significant intercept, indicating their average behavior to be aligned with the whole average summed landslide size across the 25 earthquake cases.

As for the significant cases, a distinction should be made between

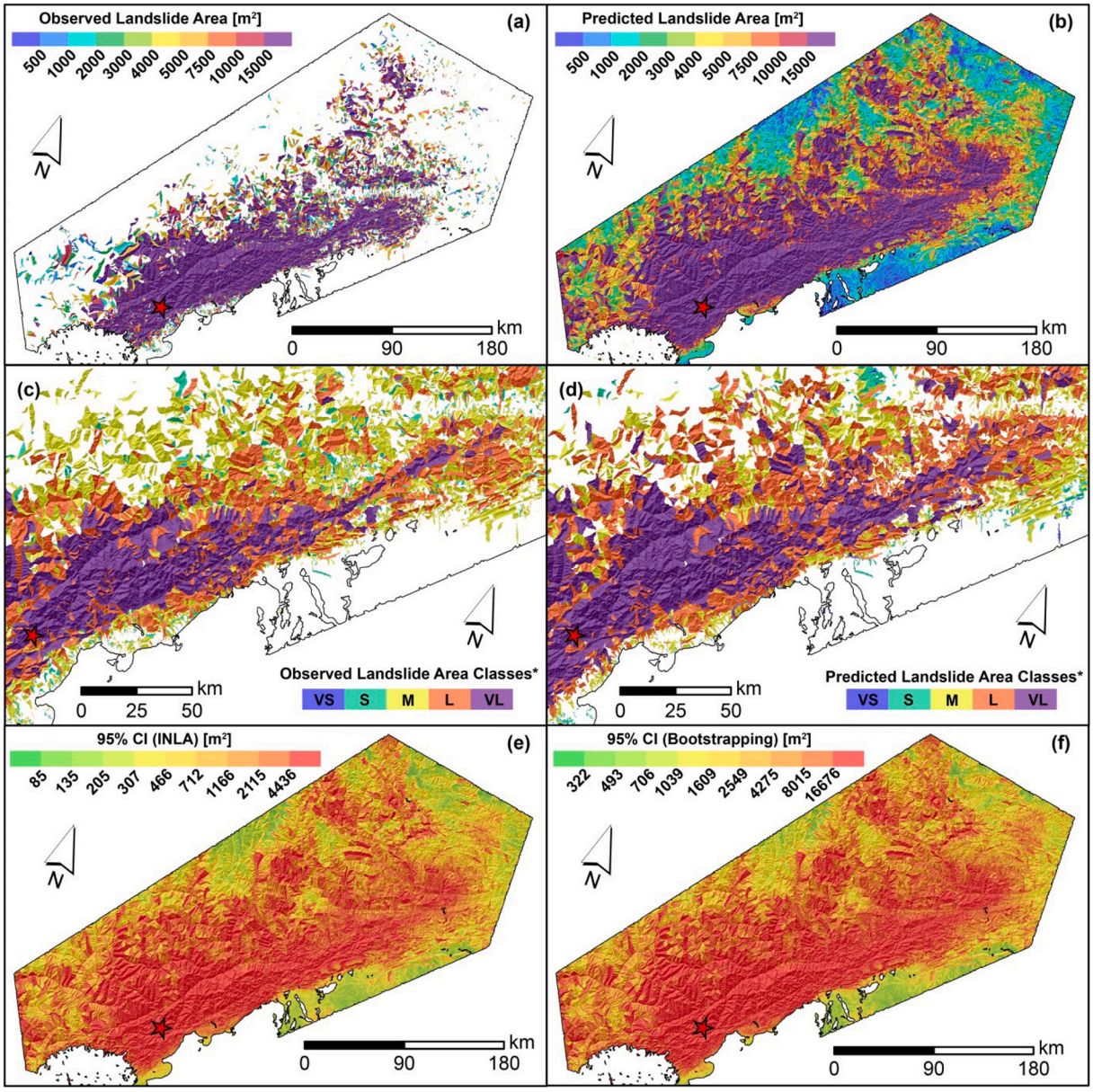

Fig. 10. Excellent agreement example for Wenchuan Sum maps: (a) Observed summed landslide area per SU. (b) Predicted mean of summed landslide area per SU. (c) Classified observed sum of landslide area per SU. (d) Classified predicted mean of summed landslide area per SU. (d) 95% credible interval estimated with INLA. (e) 95% credible interval estimated via bootstrap.

positive and negative multiple intercepts. A positive regression coefficient implies that for the earthquake under consideration a regression constant should be added to the model to increase the estimated landslide size (whether it is for the Max or Sum models) with respect to the average landslide size for all the 25 cases combined. For the Max model, ten intercepts are significant and positive. By sorting them according to their posterior mean, we can list: Guatemala, Denali, Lefkada, Chi-Chi, Iwate Miyagi, Limon, Ludian, Northridge, Wenchuan and Kiholo Bay. Similarly, ten more events have been estimated to be significant and negative overall. These can be sorted again in decreasing order from Gorkha to Friuli, Kobe, Yushu, Tohoku, Kashmir, Sierra Cucapah, Minxian, Lushan and Haiti.

An analogous situation can be found for the Sum model although the events with a significant and positive regression constant are 13 and those that are significant and negative are eight. Sorting for their posterior mean regression coefficients, to the positive category belong: Guatemala, Ludian, Iwate Miyagi, Northridge, Limon, Wenchuan, Lefkada, Denali, Coalinga, Chi-Chi, Minxian, Lushan and Haiti. As for the negative counterparts, the eight earthquakes sorted in descending order of contribution to the landslide size are: Gorkha, Friuli, Kashmir, Yushu, Tohoku, Sierra Cucapah, Kobe and Pisco.

These significant regression coefficients could be associated with both site-specific factors and/or quality of landslide inventories. Hence, they may be sensitive to real landslide size characteristics but also to landslide positional and mapped extent biases (Steger et al., 2016). Denali is one of those cases where the significant and positive intercept is relatively easy to justify. In fact, Jibson et al. (2004) already stated that the 2002 Denali earthquake had significantly lower concentrations of small landslides (rock-falls and rock-slides) compared to an earthquake with comparable or lower magnitude. Their interpretation was mainly due to the ground motion characteristics of the Denali earthquake. Furthermore, they argued that the reason was the deficiency in high-frequencies and high-amplitude accelerations of the seismic shaking. Conversely, a significant regression constant could also be

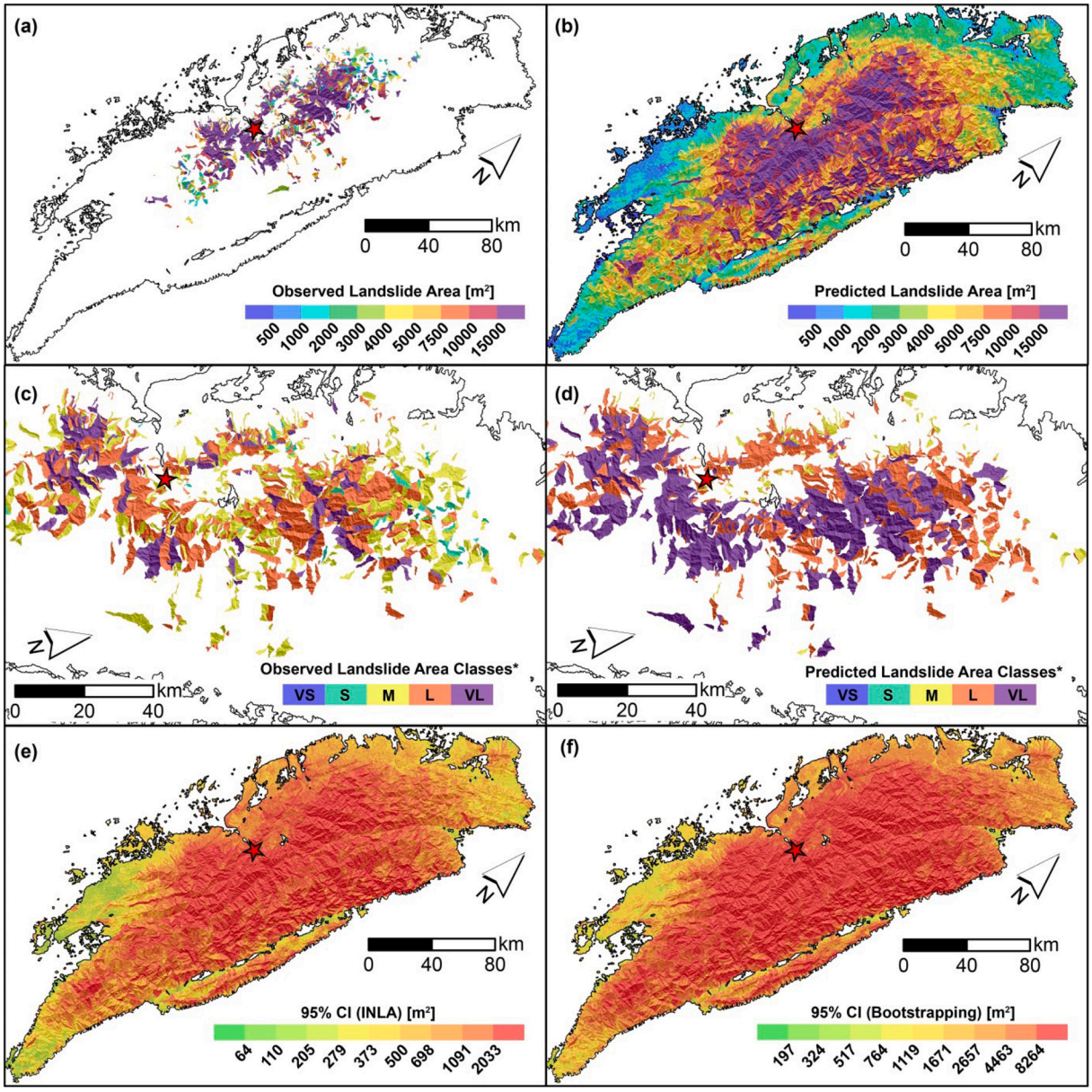

Fig. 11. Acceptable agreement example for Chi-Chi Max maps: (a) Observed maximum landslide area per SU. (b) Predicted maximum landslide area per SU. (c) Classified observed maximum landslide area per SU. (d) Classified predicted maximum landslide area per SU. (d) 95% credible interval estimated with INLA. (e) 95% credible interval estimated via bootstrap.

associated with the quality of dataset. For instance, the Limon inventory is another case where we observe a significant and positive regression constant. We recall here that the inventory was mapped by Marc et al. (2016) using 30 m resolution satellite scenes (see Table S1). Notably, mapping landslides using relatively coarse resolution images can induce substantial amalgamation issues in the delineation of large landslides. Therefore, the multiple intercept for Limon could be due to the large size of the landslides, because anything below a 900 m^2 pixel was not even visible during the mapping procedure. Therefore, here we make the point that the quality (Guzzetti et al., 2012) of an inventory could affect the estimates of each regression constant per earthquake. But, this effect can still be traced back and interpreted.

This is not exactly the case for the completeness (Guzzetti et al., 2012) of an EQIL. Tanyaş and Lombardo (2020) proposed a semi-quantitative routine to assess the completeness of the same coseismic landslide inventories used in this work (see Figure 5 in their work). If our model would have strongly suffered from a bias brought by the varying completeness associated with each of the 25 inventories, then one could have expected good inventories to share a common multiple intercept sign and/or amplitude and vice-versa in case of bad inventories. Fortunately, mixed completeness levels are featured in sub-groups of earthquakes associated with positive and negative regression constants. In turn, we can assume that a marked bias towards good or bad inventories should not be assumed for the Max model.

Even for the Sum model, the completeness of each corresponding inventory largely varies between positively and negatively attributed regression constants per earthquake events. This means that a strong influence of the completeness bias should not be present even in our Sum model, although quality-wise the effect can still be present. Such considerations are not new to the landslide literature, and we refer the reader to Steger et al. (2017, 2021) for further details on the biasing effects of incomplete inventories.

This being said, it is inevitable that several sources of bias have made their way into our model, and they will be further discussed in Section

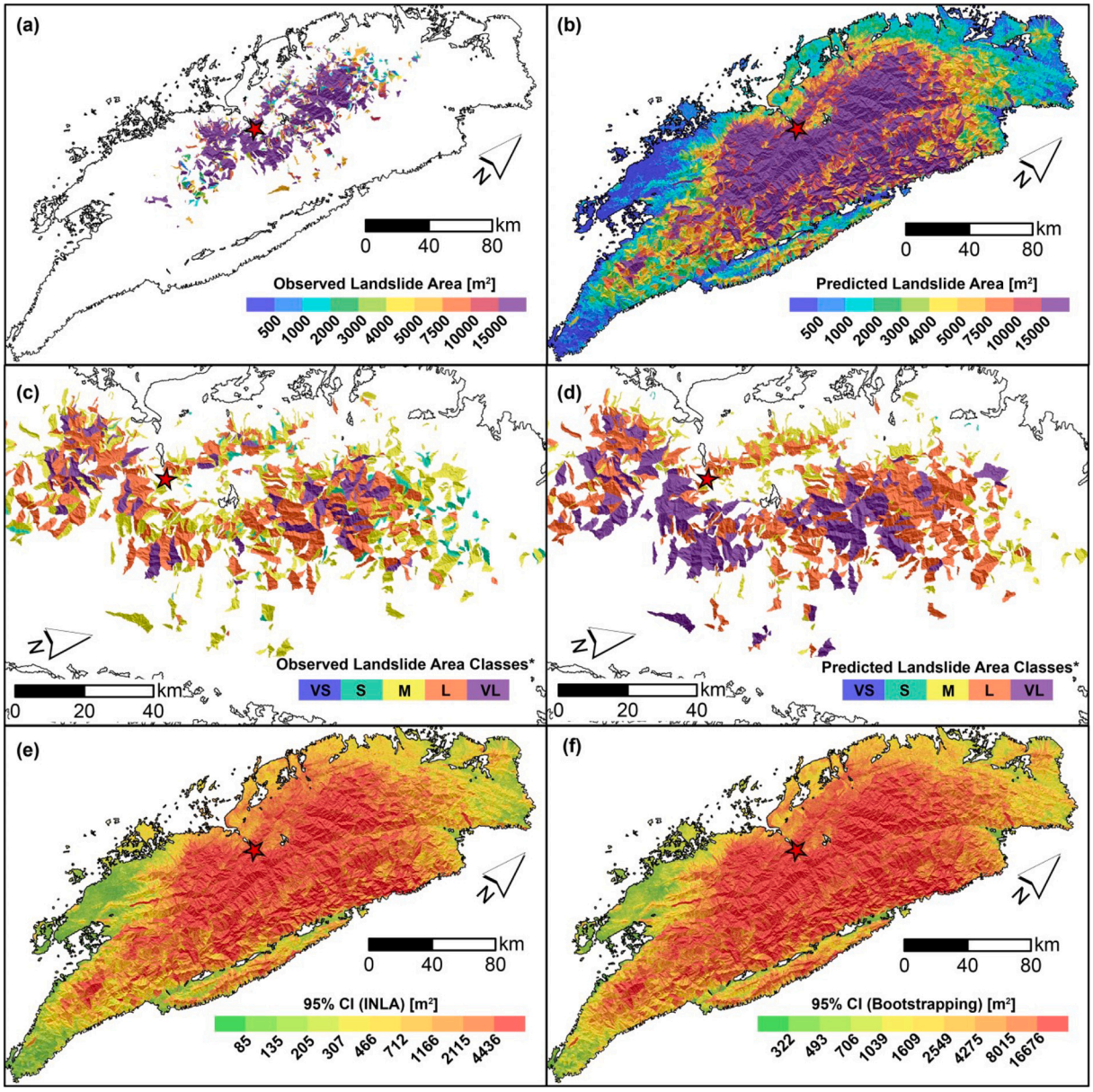

Fig. 12. Acceptable agreement example for Chi-Chi Sum maps: (a) Observed summed landslide area per SU. (b) Predicted mean of summed landslide area per SU. (c) Classified observed sum of landslide area per SU. (d) Classified predicted mean of summed landslide area per SU. (d) 95% credible interval estimated with INLA. (e) 95% credible interval estimated via bootstrap.

6.3.

Another iid effect in our model corresponds to the landform classification. We have initially made the expert choice of selecting three properties and use them as random effects whereas all the remaining linear covariates have then been selected on the basis of a variable selection procedure. Therefore, we have kept the landform classification in the model although, as also visible in Fig. 5b, none of the landform classes play a significant role, nor exhibit a posterior mean coefficient large enough to assume that its inclusion would actually play any role at all in modelling landslide sizes.

Two considerations must be made here. First of all, whether the landforms are featured in the model or not, as they are expressed, the results will essentially stay the same. We have actually re-run a set of tests that confirm this statement (unreported results). However, to avoid re-computing the fits, the 5000 simulations and the Bootstrap step, both for Max and Sum models, we have opted to keep the landforms in. The second consideration consists of assessing why such a covariate, usually quite important in landslide predictive models, has a negligible contribution to the landslide areas. We will start by saying that for consistency reasons we used the same landform classification adopted in Tanyaş et al. (2019a). In this work, the authors used the same SU partition and co-seismic landslide inventories for building a global susceptibility model. Moreover, they derived only five grouped landform classes. This could have smoothed out the signal of different landform categories to the point where both Max and Sum models may not be able to capture any dependence with respective to the landslide size. Also, a landform classification reflects several aspects of the terrain morphometry, which could have been better explained via numerical covariates such as relief, slope and curvatures, rather than in a categorical form. This being said, we stress that the Max and Sum models are essentially unchanged whether the landforms are featured or not, and yet the overall performance is more than satisfactory. Ultimately, we would like to further comment on the nonlinear effect of the *Slope (avg)*. Fig. 5c shows two slightly different patterns for the Max and Sum models. They both

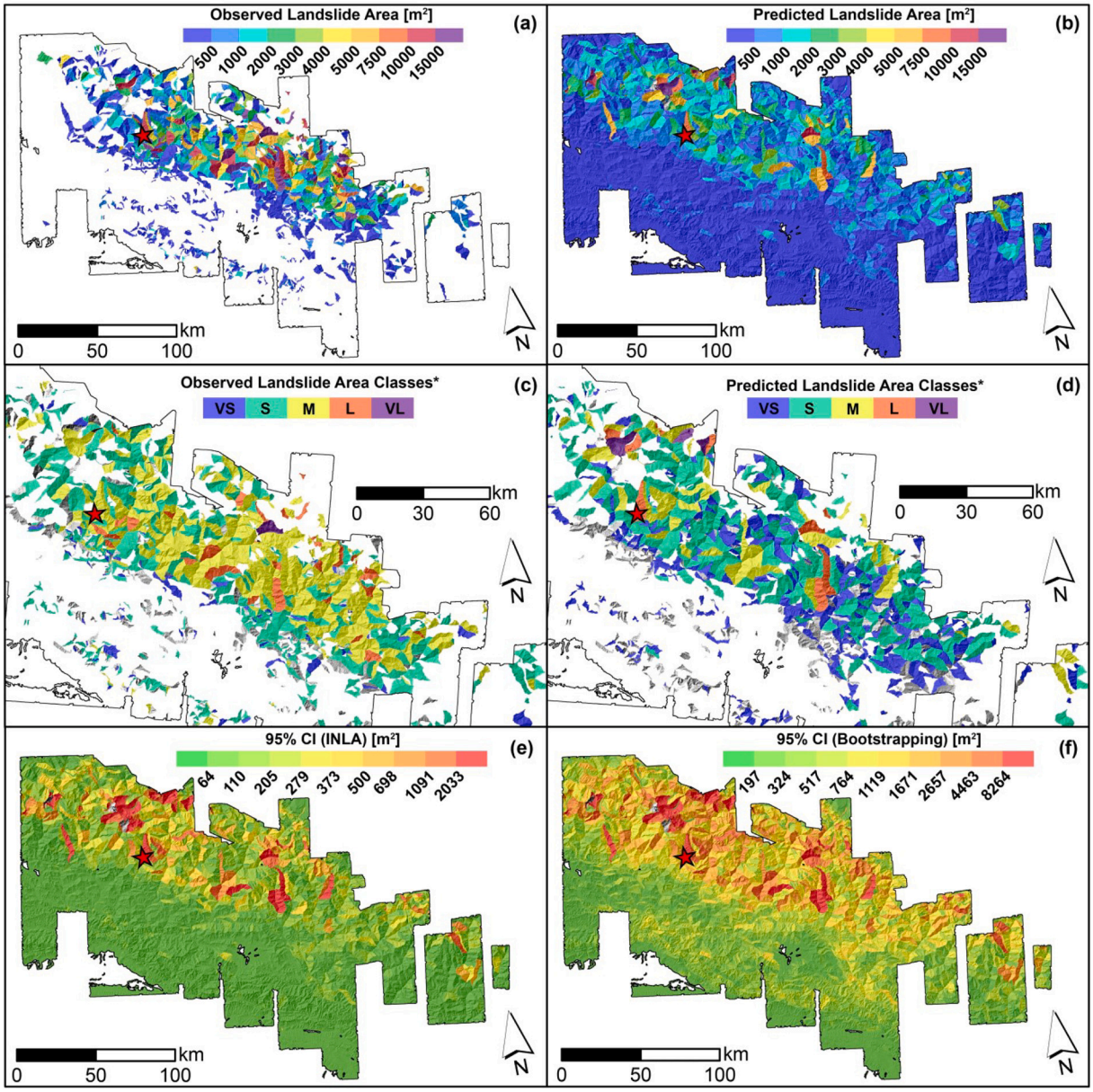

Fig. 13. Acceptable agreement example for Gorkha Max maps: (a) Observed maximum landslide area per SU. (b) Predicted maximum landslide area per SU. (c) Classified observed maximum landslide area per SU. (d) Classified predicted maximum landslide area per SU. (d) 95% credible interval estimated with INLA. (e) 95% credible interval estimated via bootstrap.

appear to play a negligible role in explaining the variability of the landslide sizes up to approximately 30 degrees of SU average steepness. From this threshold onward, the *Slope (avg)* effect becomes slightly positive for the Max model and it becomes positive and much larger for the Sum model. The difference between the two models is subtle but essentially one can see the Sum model to be characterized by larger landslide planimetric areas compared to the Max model. Therefore, a much steeper trend in the regression coefficients of the Sum model can be explained with a greater need of a SU to be steep for it to generate larger mass movements.

6.3. Sources of uncertainty

A large number of uncertainty sources inevitably affect our co-seismic landslide datasets. The main sources of uncertainty essentially boil down to the quality, completeness and representation of the co-seismic landslide inventories (Guzzetti et al., 2012; Tanyaş et al., 2017). Below, we list potential biases associated with the three concepts mentioned above, and further below we will provide our interpretation of the resulting bias.

- composition of the team mapping the co-seismic landslide inventories.
- the quality of the support data upon which the mapping is undertaken.
  - spatial resolution. Is it fine enough to be able to map?
  - temporal resolution. Is it sufficiently close to the earthquake occurrence or is it far and therefore potentially containing subsequent unrelated landslides?
  - are the satellite scenes covered by clouds?
  - is the extent of the satellite imagery comparable to the extent of the landslide-affected area?
- the technique used for mapping

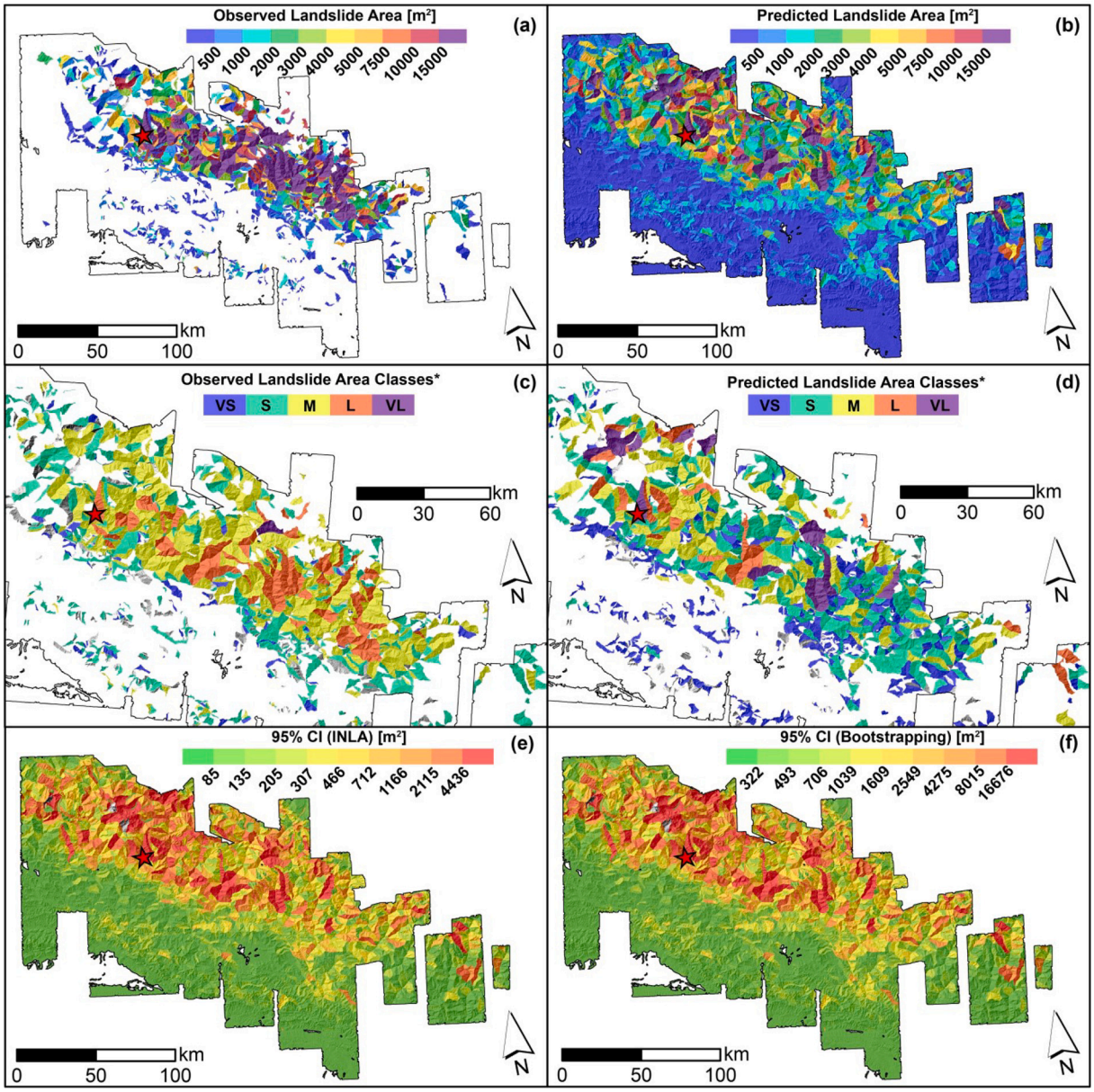

Fig. 14. Acceptable agreement example for Gorkha Sum maps: (a) Observed summed landslide area per SU. (b) Predicted mean of summed landslide area per SU. (c) Classified observed sum of landslide area per SU. (d) Classified predicted mean of summed landslide area per SU. (d) 95% credible interval estimated with INLA. (e) 95% credible interval estimated via bootstrap.

  - the subjectiveness of the mapping itself in case of manually digitized inventories.
  - the error in the automatic or semi-automatic mapping procedure.
- minimum resolved landslide size.
- the classification (or not) of each landslide according to its types.

The quality of landslide inventories could bring some uncertainties into spatial distribution of co-seismic landslides' size. In this regard, amalgamation of coalescing or adjacent landslides is an issue that typically affects any estimate of landslide sizes, but the level of amalgamation can also vary on the basis of: (i) mapping techniques, (ii) spatial and (iii) temporal resolution of examined scenes (Tanyaş et al., 2019b).

Overall, manual landslide mapping is subjective and the final product varies based on mapping objectives, preferences and/or skill of the interpreter(s) and the time invested in the inventory (Soeters and Van Westen, 1996). Obviously, the database we used in this study includes landslide inventories compiled for different purposes, through various methods and expertise in the 40-year period from 1976 to 2016. With the exception of the Pisco inventory, created via semi-automated mapping routines (Lacroix et al., 2013), all the inventories were mapped manually. Therefore, it is not a homogeneous dataset. Given this limitation, the multiple intercept we included in our models is a way to cope with such uncertainties. For instance, landslides triggered by the Gorkha earthquake were mapped (Roback et al., 2018) not only to assess the landslide hazard but also to examine mobility of landslides. In turn, Roback et al. (2018) paid an extra attention to amalgamation issues and they even differentiate landslide source and deposit. This could partly explains the significant and negative regression coefficient we calculated for the intercept of the Gorkha case, which is the most striking example among multiple intercepts per earthquake. In fact, Fig. 5 reports the largest (in absolute value) posterior mean of the regression coefficient distribution for Gorkha, that the model uses to reduce the estimated landslide size for this particular earthquake. We should also

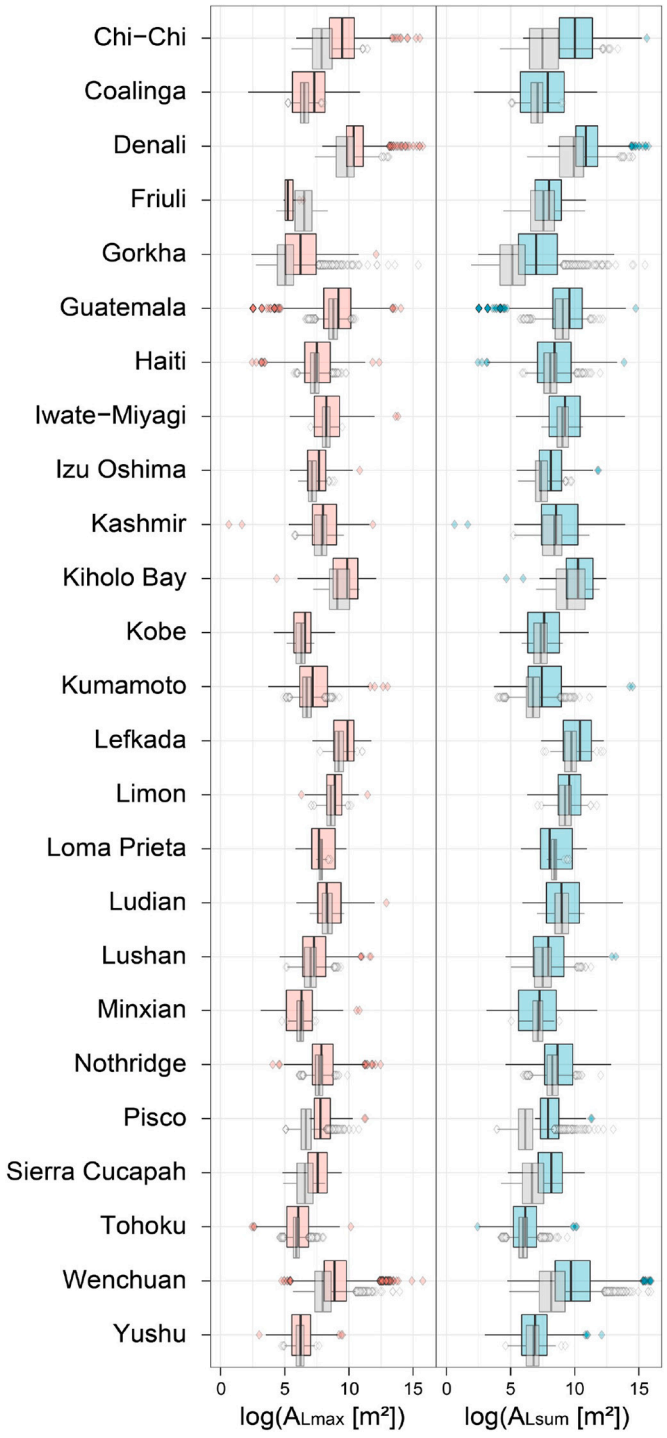

Fig. 15. Distribution of the posterior mean of landslide sizes per SU, for the Max (pink boxplots) and Sum (cyan boxplots) models. The grey boxplots correspond to the observed log(A_L). (For interpretation of the references to color in this figure legend, the reader is referred to the web version of this article.)

note that this may not be the only interpretation available. The reasons behind it, may also be due to additional seismo-tectonic or ground-motion related factors. And, disentangling the main reason to which extent one cause or the other may be responsible for such a small intercept certainly requires further investigation, even beyond the scope of this work. In either case this particular earthquake was already pointed out to have produced less landslides than the expected number for a comparable magnitude (Kargel et al., 2016; Xu et al., 2016). Moreover, our model adds to this observation, stressing that not only the number of landslides is smaller than other earthquakes, but that this is valid also in terms of planimetric areas.

In addition to mapping techniques, the spatial resolution of the satellite images or orthophotos used to support the mapping itself also effects the level of amalgamation (see the details provided for the Limon case in Section 6.2). Whenever supporting images with high spatial resolution images are used, the ability to characterize small landslides also increases. Therefore, positive or negative regression coefficients associated with each multiple intercept may also be due to this. Haiti is again a good example for a such case. The landslides triggered by the Haiti earthquake were mapped using scenes with a spatial resolution of less than 1 m (see, (Harp et al., 2016) for details and Table S1 for comparison with other inventories). In this regard, we consider the Haiti inventory to be effected by amalgamation to a much lesser extent than most of the other inventories we used.

Moreover, in some cases, if the time gap between pre- and post-seismic images is relatively long, some pre-seismic landslides could be included into the co-seismic landslide inventory by mistake (Tanyaş et al., 2017). This may also lead to map reactivation or expansion or pre-earthquake landslides including the whole landslide scar rather than the newly failed surface. In turn, this may bias the A_L towards much larger estimates than what they should be in reality.

Moreover, the global nature of our dataset incorporates all the above inventory-specific issues. Therefore, biases can arise from their combined co-existence in our Max and Sum models. For instance, inventories containing a much larger landslide population may bias the final predictive model at the expenses of inventories represented by fewer landslides. In this complex system of potential bias interactions, we should also mention that another possible source of bias may exist and it may have directly affected the way we constructed our global dataset. In fact, the Slope Unit partition controlled the landslide area aggregation when we computed the Max and Sum out of the multiple landslides per mapping unit. In this sense, to generate a number of SUs for which a global landslide model can be efficiently built, Tanyaş et al. (2019a) chose a relatively coarse parameterization of *r.slopeunits*—we recall here that the SUs we used are the same as those generated by Tanyas and co-authors. However, a much finer and realistic SU subdivision can still be made, which we expect would substantially improve the Max and Sum models' performance. This being said, we should also report that the selected *r.slopeunits* parameterization has been consistent among different earthquakes. This ensures that whatever bias may exist because of the coarse dimension of the SUs, it would be consistent and relatively constant across our entire global dataset. Furthermore, the way we computed the landslide area could be a source of bias, albeit to a minor extent. In fact, the planimetric extent of landslides could have been topographically corrected as per Steger et al. (2021). However, due to the fact that two of our inventories were point-based and the landslide areas were already reported in the attribute table, we opted to consistently measure the same quantity also for the remaining inventories.

Ultimately, it is fair to report that the covariates themselves may bring some degree of uncertainty. In fact, the resolution among covariates substantially changes, starting from a fine representation of terrain properties at 30 m and ending up to the 1 km resolution of the ground motion properties. However, similarly to the Slope Unit dimension case, the difference in resolution among covariates is constant in our global dataset.

6.4. Considerations on modelling landslide areas

Our model has a specific limitation. We model the planimetric area of landslides on a logarithmic scale. Our model overall performed well in such scale but in order to produce practically interpretable results or maps, we should convert our prediction back into a metric unit. We recall here that as most of the Gaussian models do, we performed much better around the bulk of the landslide area distribution rather than in

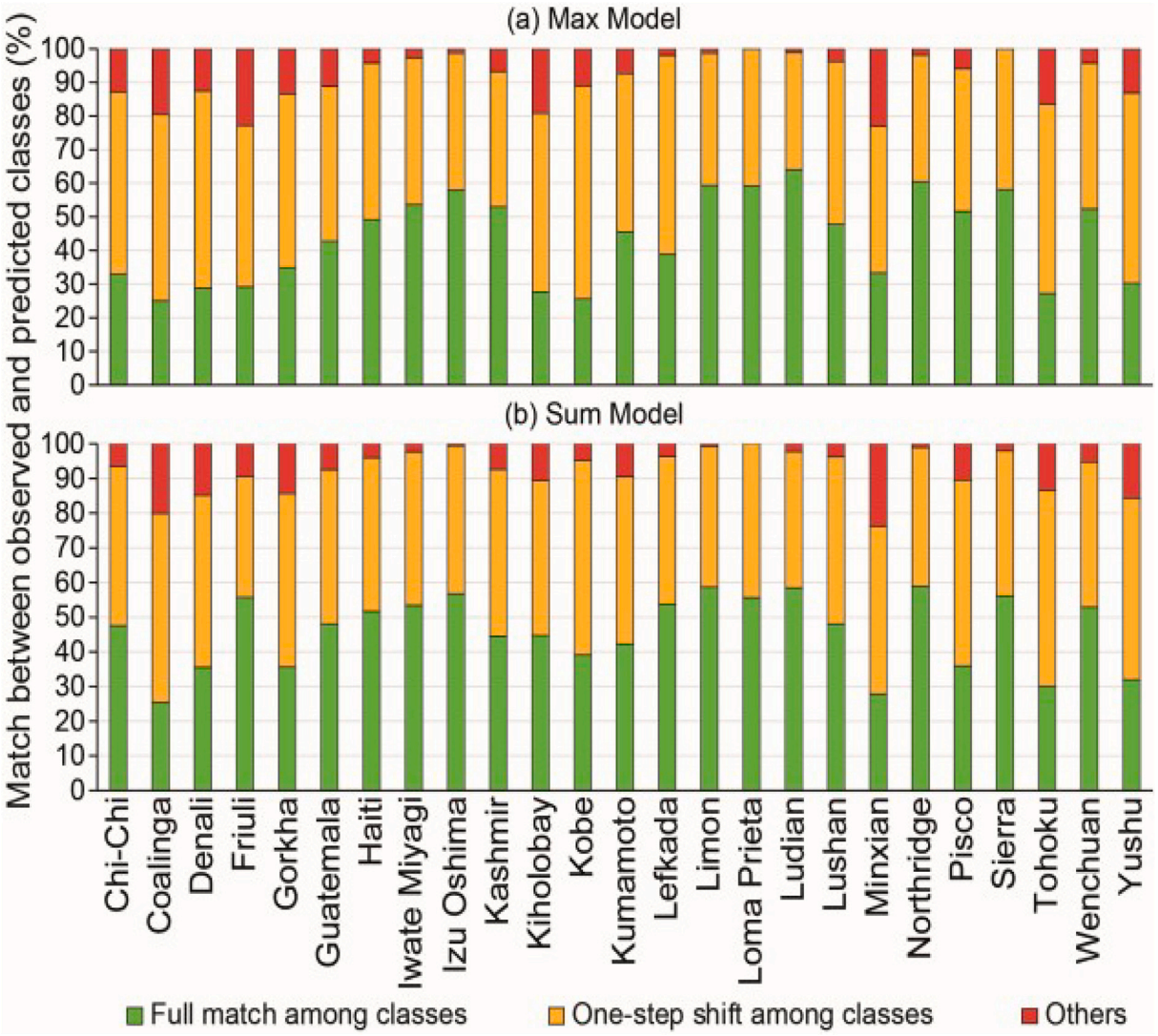

Fig. 16. Stacked barplot reporting the percentage of cases—with respect to the total for each earthquake—for which the observed and predicted classes of landslide area coincide (green), are shifted by a single class (orange) and are shifted by two classes (red). (For interpretation of the references to color in this figure legend, the reader is referred to the web version of this article.)

the tails. Therefore, converting our prediction from the logarithmic to the actual meter scale would exacerbate the difference between (very small and very large) observed and estimated landslide areas. It is worth noting that this problem exists in most Log-Gaussian models and even in the context of landslide-event magnitude scale. In fact, the same logarithmic representation and associated limitations affect landslide magnitude studies, where frequency-area distributions are modelled in log-scale rather than the metric one (Malamud et al., 2004a).

Another potential difficulty is that the mean of A_L is *not* equal to the exponential of the mean of $\log(A_L)$, which makes the interpretation of results more intricate. However, the logarithm being a monotone increasing function, it respects the transformation of quantiles from one scale to the other (*e.g.*, the median of A_L is equal to the exponential of the median of $\log(A_L)$). Therefore, in two theoretical maps where the landslide size is predicted per SU, the relative classes would be visually maintained in both metric and logarithmic scales.

The landslide area classification we explain in Section 5.4 and show in Fig. 6 is meant to limit the issues between the two scales. The overall agreement between observed and predicted landslide classes shows the success of this classification approach (see Fig. 16). On average, observed and predicted landslide classes perfectly match for 44% and 46% of examined mapping units for Max and Sum models, respectively (these values correspond to the average height of the green barplots in Fig. 16). As for an average percentage of strongly mismatching case, only 7% of predicted landslide sizes is associated with a two-class shift, both for the Max and Sum models (these values correspond to the average height of the red barplots in Fig. 16).

6.5. *Implications for landslide hazard assessment*

The method we propose is the first of its kind. Therefore, the implications it may produce to the landslide hazard concept are still to be investigated. For sure, this globally-applicable model has provided the first predictive maps of the potential landslide area generated in response to an earthquake. This information only answers to one of the three components of the landslide hazard concept, this being how large a landslide-event may be spatially. However, our model, as we defined it, is tightly linked to the ground motion patterns of past earthquakes. Therefore, there is no guarantee that future earthquakes will produce analogous shaking levels and thus, our current landslide size maps are mostly reflecting what happened in the past. We envision two extensions of our model for it to become fully operative. One way is to feature a probabilistic term for the seismic hazard. For instance, once our model has been built and the regression coefficient for the Macroseismic

Intensity is available, then any other Macroseismic Intensity (*e.g.*, exceedance in 10 or 50 years return time, Giardini et al., 1999; Jordan et al., 2014) map can be plugged in Lombardo and Tanyas (2020) to produce scenario-based outputs (Lombardo and Tanyas, 2021). These scenario-based maps could then be integrated in the decision-making procedure for medium to long term territorial planning.

Conversely, another possible alternative is to use our model in near real-time. As before, the regression coefficients of all covariates, including the Macroseismic Intensity can be kept fixed and right after a future earthquake, the associated Macroseismic Intensity can be plugged in to provide quick post-disaster information on landslide sizes. Nowadays, the United States Geological Survey is able to provide reliable shaking level maps within hours after a major earthquake (Allstadt et al., 2018) and therefore our model could rapidly provide estimates of how large the resulting landslides might be, and how they might be distributed over space.

It is also important to stress that our model is valid only for earthquake-induced landslides. However, we limited our scope to this specific class of trigger because of the global availability of the data. An analogous model could be replicated for rainfall-induced landslides and also for a mixture of both trigger types. Nevertheless, a proportionally large global inventory should be made for the precipitation case.

As mentioned above, to date, no statistically-based spatially-explicit model was able to predict landslide planimetric areas, or their aggregation in a given mapping unit. Therefore, there is no landslide hazard guideline where the use of the model we propose is clearly defined. And yet, in landslide hazard assessment, the frequency-area distribution (Malamud et al., 2004a) derived for a landslide event of a given magnitude is measured as a function of the overall number of landslides and their associated planimetric areas, produced by a given trigger.

Our model can offer additional information to two key tools in landslide hazard assessment. In addition to the prediction of landslide occurrence locations (susceptibility, Reichenbach et al., 2018), and to the estimation of how many landslides may trigger per mapping unit (intensity, Lombardo et al., 2018a), our model can inform decision makers on the extent of the failed surface per slope unit.

Furthermore, in the traditional literature of landslide predictive models, the most common mapping units are grid cells and slope units. However, the model we propose is not suitable for a grid cell spatial partition. In fact, we need to express the landslide size at a scale comparable or larger to the actual landslides. Therefore, grid cells, which are typically much smaller than a landslide, cannot be used. Moreover, in case one would like to generate a squared lattice with a size larger than a landslide, then we stress here that the geomorphological significance will be mostly lost. This is also true for susceptibility studies because a single pixel does not represent the geomorphological process behind a landslide. However, it is even more true and strict when modelling landslide planimetric areas. This is not the case for SUs. Geomorphologically, a slope unit is a medium scale representation of the landscape, positioned in between the fine grid cells—often criticized for the same reason mentioned above, *e.g.*, Reichenbach et al. (2018)—and the catchments—undoubtedly too coarse to be effective for slope stabilization practices. Therefore, at least theoretically a SU partition offers an operational spatial scale upon which the method we propose can be repeated for any other area and/or landslide type. Therefore an additional map predicting SU-based landslide Max or Sum scenarios could become a new tool in landslide hazard mapping. As for a catchment partition, this could still be theoretically doable but the representation of the covariates at such scale may lose connection or correlation with respect to the A_L. For instance, the average slope steepness in a given catchment may be totally unrelated to the landslide planimetric area at a single slope.

6.6. Statistical considerations

We have developed a probabilistic, likelihood-based approach to model landslide sizes under the assumption that a latent structure drives all the trends and dependence patterns we observe in our data. Contrary to the widely-used frequentist approach, we opted for a Bayesian approach and used INLA for inference. The main advantage of Bayesian approaches is that past knowledge of the observed process can be encoded into a probabilistic element known as a prior distribution. The prior is combined with the information extracted from the data to draw conclusions about the observed process. Additionally, by using a Bayesian approach through INLA, it is possible to handle uncertainty estimation and prediction over space in a very elegant and numerically convenient way. Non-Bayesian solutions for inference with latent variables can also be implemented through, *e.g.*, the Expectation-Maximisation (EM) algorithm.

Although our modelling approach represents an important contribution to landslide hazard modelling, many improvements can already be envisioned from a statistical perspective.

First, our focus here is to model and predict the size of landslides only, but a joint modelling approach could have been considered to simultaneously model both the landslide susceptibility (Reichenbach et al., 2018) and size, or landslide intensity (Lombardo et al., 2020a) and size. In particular, the INLA approach offers a suitable statistical framework where different likelihoods can be assumed for different responses sharing common features (see, *e.g.*, Krainski et al., 2018, Chapter 3).

Second, our modelling approach is not "strictly spatial" in the sense that—for fixed covariate values—it does not define a correlation or covariance structure between observations in neighboring SUs. In other words, our Max and Sum models treat close-by and far away SUs equally. While such an assumption is reasonable from a computational perspective, it also means that we are unable to capture spatially structured effects that are not already captured by the available covariates. If such unobserved spatial effects are strong and not accounted for in the model, this might bias the estimated covariate effects and might even in some cases affect their geomorphological interpretation. Fortunately for us, as shown by Lombardo et al. (2019a), the *Macroseimic Intensity (MI)* covariate is a good proxy for the trigger and usually provides similar information as a model for EQILs that would include a latent spatially-correlated effect (Lombardo et al., 2018a). Therefore, we can here reasonably assume, and be confident that by including the *MI* and related covariate information in our model, the residual spatial correlation is quite weak overall, though this would need to be checked more systematically and thoroughly. For rainfall-induced landslides, however, it is usually much more difficult to obtain relevant covariates representing the trigger at high resolution, and for such data, additional latent spatial effects (specific to each event) would seem necessary. Such a spatial model defined at the latent level can be constructed using the stochastic partial differential equation (SPDE) approach that provides accurate Markovian representations of the flexible Matérn covariance (see Schabenberger and Gotway, 2017, Chapter 4 for an introduction on covariance functions and Castro-Camilo et al., 2020 for the use of the SPDE approach in a prediction framework). For the dataset used here, a sensible approach is to assume different SPDE models for each earthquake inventory, which helps us reduce the computation burden. However, even doing so, this modelling approach carries significant computational challenges (Castro-Camilo et al., 2020), and simpler spatial structures could be envisioned, *e.g.*, using the Besag model for areal units as in Lombardo et al. (2018a).

Third, although the inventories used in our work correspond to spatially replicated events around the world, we could focus on a single area instead, where multitemporal inventories are available. Under such a setting, spatio-temporal models based on a Log-Gaussian likelihood can help us describe the spatial extent of landslides and their evolution in time. Space-time landslide intensity models were fitted by Lombardo et al. (2020a) and it would be interesting to generalize their approach to model the spatio-temporal evolution of landslide sizes, potentially jointly with their occurrence locations. Moreover, the SPDE approach

mentioned earlier can also be extended to describe processes evolving in space and time using separable covariance structures (Gneiting et al., 2006). It is important to notice, however, that the computational gains obtained through the reduction in spatial coverage are counterbalanced by the complexity associated with spatio-temporal models; therefore, it is difficult to assess the computational requirements in advance.

As mentioned above, our model is not spatial in the sense that it does not account for the spatial relationship between slope units. Ignoring spatial correlation would make estimates' posterior standard deviations too small. A spatial model would reduce the effective sample size since realisations that are spatially correlated reduce their contribution as they provide similar information. Nonetheless, such spatial analysis will have little effect on the estimates (Chapter 9 Hodges, 2013). Therefore, the main difference between a model such as ours and a model that includes spatial interactions lies in the uncertainty quantification of the estimates. The parametric Bootstrap methodology is one way to compensate for this and to quantify the potential uncertainty underestimation. Indeed, it can be perceived as a post-processing step of the fits, where resampling techniques are used in order to construct many new data samples that, in turn, can be used to refit several models. The estimates extracted from each new fit are then used to compute sample standard deviations for the original estimates. Although this process is more computationally demanding, it guarantees a more realistic uncertainty quantification. This means that Bootstrap-based standard deviations can in some cases be fairly large compared to their INLA counterpart, as can be observed in Figs. 7–14.

6.7. Computational requirements

The models used here for $A_{L_{\max}}$ and $A_{L_{\text{sum}}}$ can be fitted using cutting-edge computers running any of the standard operating systems currently available. RAM requirements are usually linear in the number of INLA threads, which is a parameter that can be specified with the main INLA function. In our case, the models were fitted using a CentOS 7 Linux computer with two threads. RAM usage was less than 1 Gb for INLA alone, which means that additional RAM should be considered to, *e.g.*, run the R software. Model fitting and prediction took approximately 10 min for both models.

The Bootstrap procedure consisted mainly of two stages. The first one (creating the Bootstrap samples) took approximately 3.2 h, while the second one (fitting models using Bootstrap samples) took roughly the same time as for the original fits, for each model and each of the 300 Bootstrap samples. The first stage can be fitted using a state-of-the-art laptop or desktop computer, but the second stage requires additional computational power and can easily exploit parallel computing. We used resources for distributed computers to speed up the Bootstrap samples fits, using CentOS 7 Linux workstations. Again, for every single fit, less than 1 Gb was required for INLA alone.

A key element at the core of the INLA algorithm is numerical linear algebra for large sparse matrices, which take most of the total runtime. For a spatial model with $|\mathcal{S}| \sim 10^5$ or less data points, these operations can be handle by INLA thanks to an internal parallelisation using OpenMP (Van Niekerk et al., 2019). For greater $|\mathcal{S}|$, additional parallel numerical methods for large sparse matrices are needed. The current R-INLA implementation allows the use of the PARDISO library, which is a powerful memory-efficient software for solving large sparse linear systems of equations. Its integration with INLA further increases INLA capability to solve very high-dimensional problems (Van Niekerk et al., 2019), such as the one we will face using landslide inventories with a more refined SU partition. Further runtime reductions can be achieve using any of the less accurate approximations methods provided in the R-INLA library (Rue et al., 2017).

6.8. Future extensions

The model we present has been built on the basis of global EQILs but it is not bound to the global nor to the co-seismic context. Its structure is applicable to any landslide hazard and for this reason, we envision to extend the very same model in few but precise directions:

- Application to specific landslide types.
- Application to any scale, from the catchment to the global levels.
- Application to rainfall-induced landslides.
- Application to snow-melt-induced landslides.
- Application to co-seimic, rainfall-induced and snow-melt-induced landslides altogether.

The current dataset could not discriminate between landslide types. Therefore, the uncertainty due to the difference in failure mechanisms among landslides has inevitably propagated into our result. However, we expect that a much more precise outcome could be achieved by modelling the planimetric area of landslides that share a common physical behavior. In turn, this will also enable landslide-class-specific interpretations and considerations that could better inform decision makers. For instance, one could estimate the potential landslide planimetric area to be triggered per SU in a specific site, and examine the expected $\log(A_L)$ for rockfalls and debris-flows separately.

Moreover, one of the problems in this work is the global nature of the dataset that we used. However, one could opt to model the $\log(A_L)$ at any other scale, from the fine catchment level, to the coarser regional or national scale. This would likely get rid of the necessity for a multiple intercept, making future models potentially more spatially or temporally transferable.

The present model can be applied to rainfall-triggered landslides. The structure could be left unchanged whereas the covariate selection could certainly vary by removing the ground motion, both *MI (avg)* and *MI (std)*, and/or adding the spatial signal of the rainfall discharge, if available. The same is valid for snow-melt landslide inventories.

Ultimately, we also envision a possible application of statistical models that can contextually distinguish the landslide size to the class of the landslide itself. Such models will represent an extension to the present case where a single likelihood for the $\log(A_L)$ is taken into consideration. Such extension would require statistical models that can take on multiple likelihoods also referred to as joint-probability models.

7. Conclusions

Fulfilling the standard definition of landslide hazard requires the expectation or prediction of where, when or how frequently a population of landslides may occur, as well as how large the landslide population may be. The way that the geoscientific community—at least the part of the community working on statistically-based hazard models—has interpreted the term "how large" for decades, is to estimate the event landslide magnitude, an index of how many and how large the total number of landslides may be. As a result, by providing a single number to represent the landslide-event-magnitude, the community has disregarded the geographic characteristic of the landslide size information. In other words, maps capable of statistically estimating the expected extent of a failing slope are not available at present. Our work, fills this gap and it is aimed to provide an additional tool both for academic researchers as well as the public. The current way governmental agencies manage the territory for landslide risk prevention is to use susceptibility maps, which convey the information about where landslides are expected to trigger. Therefore, our Max and Sum models could be considered a complementary resource to improve operational decisions in territorial management protocols. By additionally considering the expected extent of a failing slope, together with the probability of a given slope to fail in the first place, much better decisions could be made to ensure the safety of human infrastructure and lives. We conclude by pointing out two elements that will certainly require further efforts in the coming future. The use of a log-Gaussian model may misrepresent extremely large landslides, which in fact are those that may pose the

largest threat to communities and infrastructure. Future extensions of the present framework may involve building extreme-value models (Davison and Huser, 2015) better suited to estimate those failures that belong to the right tail of the landslide size distribution rather than its bulk. Furthermore, the landslide area may not be the best candidate to be modeled. In fact, landslide kinematic characteristics are equivalent if not more important characteristics of the hazard presented by a given landslide. However, kinematic characteristics are not available at present, but could be a further and even more meaningful extension to the present model to estimate the hazard associated to large populations of landslides.

Author statement

Luigi Lombardo, Hakan Tanyas and Daniela Castro-Camilo have initially envisioned the research.

Fausto Guzzetti and Raphaël Huser have later helped to refine the idea behind it.

Luigi Lombardo and Hakan Tanyas have pre-processed the data and contributed to the figuremaking.

Daniela Castro-Camilo have run all the analyses.

Writing and revising the manuscript has been equally shared among co-authors.

Declaration of Competing Interest

The authors declare no conflict of interest.

Acknowledgement

The authors would like to publicly thank the Editor, Dr. Janusz Wasowski, and the two reviewers, Dr. Stefan Steger and Prof. Paolo Frattini, for their suggestions to improve the manuscript. We do believe that their insightful and stimulating comments have made the manuscript much more rich and readable.

Appendix A. Supplementary data

Supplementary data to this article can be found online at https://doi.org/10.1016/j.enggeo.2021.106288.

References

Adams, P.W., Sidle, R.C., 1987. Soil conditions in three recent landslides in Southeast Alaska. Forest Ecol. Manag. 18 (2), 93–102.
Allstadt, K.E., Jibson, R.W., Thompson, E.M., Massey, C.I., Wald, D.J., Godt, J.W., Rengers, F.K., 2018. Improving near-real-time coseismic landslide models: lessons learned from the 2016 Kaikōura, New Zealand, earthquake improving near-real-time coseismic landslide models. Bull. Seismol. Soc. Am. 108 (3B), 1649–1664.
Alvioli, M., Marchesini, I., Reichenbach, P., Rossi, M., Ardizzone, F., Fiorucci, F., Guzzetti, F., 2016. Automatic delineation of geomorphological slope units with r.slopeunits v1.0 and their optimization for landslide susceptibility modeling. Geosci. Model Dev. 9 (11), 3975–3991.
Amatulli, G., Domisch, S., Tuanmu, M.-N., Parmentier, B., Ranipeta, A., Malczyk, J., Jetz, W., 2018. A suite of global, cross-scale topographic variables for environmental and biodiversity modeling. Sci. Data 5, 180040.
Bellugi, D.G., Milledge, D.G., Cuffey, K.M., Dietrich, W.E., Larsen, L.G., 2021. Controls on the size distributions of shallow landslides. Proc. Natl. Acad. Sci. USA 118 (9) e2021855118.
Beven, K., Kirkby, M.J., 1979. A physically based, variable contributing area model of basin hydrology/Un modèle à base physique de zone d'appel variable de l'hydrologie du bassin versant. Hydrol. Sci. J. 24 (1), 43–69.
Bivand, R., Piras, G., 2015. Comparing implementations of estimation methods for spatial econometrics. J. Stat. Softw. 63 (18), 1–36.
Bourdeau, C., Havenith, H.-B., Fleurisson, J.-A., Grandjean, G., 2004. Numerical modelling of seismic slope stability. In: Engineering Geology for Infrastructure Planning in Europe. Springer, pp. 671–684.
van den Bout, B., Lombardo, L., Chiyang, M., van Westen, C., Jetten, V., 2021. Physically-based catchment-scale prediction of slope failure volume and geometry. Eng. Geol. 284, 105942.
Bout, B., Lombardo, L., van Westen, C., Jetten, V., 2018. Integration of two-phase solid fluid equations in a catchment model for flashfloods, debris flows and shallow slope failures. Environ. Model. Softw. 105, 1–16.
Brabb, E.E., 1991. The world landslide problem. Episodes 14 (1), 52–61.
Brabb, E.E., Harrod, B.L. (Eds.), 1989. Landslides: Extent and Economic Significance: Proceedings 28th International Geological Congress Symposium on Landslides. Rotterdam and Brookfield, Vermont.
Broeckx, J., Rossi, M., Lijnen, K., Campforts, B., Poesen, J., Vanmaercke, M., 2019. Landslide mobilization rates: a global analysis and model. Earth-Sci. Rev. 102972.
Brunetti, M., Guzzetti, F., Rossi, M., 2009a. Probability distributions of landslide volumes. Nonlinear Process. Geophys. 16 (2), 179–188.
Brunetti, M., Guzzetti, F., Rossi, M., 2009b. Probability distributions of landslide volumes. Nonlinear Process. Geophys. 16 (2), 179–188.
Buchanan, T.J., Somers, W.P., 1976. Discharge measurements at gaging stations. In: Techniques for Water Investigations of the United States Geological Survey, Number 3 in Applications of Hydraulics. United States Government Printing Office, Washington, DC second edition.
Cardinali, M., Reichenbach, P., Guzzetti, F., Ardizzone, F., Antonini, G., Galli, M., Cacciano, M., Castellani, M., Salvati, P., 2002. A Geomorphological Approach to the Estimation of Landslide Hazards and Risks in Umbria, Central Italy. Natural Hazards Earth Systems Science.
Carrara, A., 1988. Drainage and divide networks derived from high-fidelity digital terrain models. Quantitative Analysis of Mineral and Energy Resources. Springer, pp. 581–597.
Castro Camilo, D., Lombardo, L., Mai, P., Dou, J., Huser, R., 2017. Handling high predictor dimensionality in slope-unit-based landslide susceptibility models through LASSO-penalized Generalized Linear Model. Environ. Model. Softw. 97, 145–156.
Castro-Camilo, D., Mhalla, L., Opitz, T., 2020. Bayesian Space-Time Gap Filling for Inference on Extreme Hot-Spots: An Application to Red Sea Surface Temperatures. Extremes (to Appear).
Catani, F., Tofani, V., Lagomarsino, D., 2016. Spatial patterns of landslide dimension: a tool for magnitude mapping. Geomorphology 273, 361–373.
Chen, C.-W., Oguchi, T., Hayakawa, Y.S., Saito, H., Chen, H., 2017. Relationship between landslide size and rainfall conditions in Taiwan. Landslides 14 (3), 1235–1240.
Cheng, S., Yang, G., Yu, H., Li, J., Zhang, L., 2012. Impacts of Wenchuan Earthquake-induced landslides on soil physical properties and tree growth. Ecol. Indic. 15 (1), 263–270.
Chigira, M., Yagi, H., 2006. Geological and geomorphological characteristics of landslides triggered by the 2004 mid niigta prefecture earthquake in Japan. Eng. Geol. 82 (4), 202–221.
Corominas, J., Mavrouli, J., 2011. Living with landslide risk in Europe: assessment, effects of global change, and risk management strategies. In: Documento técnico, SafeLand. 7th Framework Programme Cooperation Theme 6.
Corominas, J., van Westen, C., Frattini, P., Cascini, L., Malet, J.-P., Fotopoulou, S., Catani, F., Van Den Eeckhaut, M., Mavrouli, O., Agliardi, F., et al., 2014. Recommendations for the quantitative analysis of landslide risk. Bull. Eng. Geol. Environ. 73 (2), 209–263.
Cressie, N., 2015. Statistics for Spatial Data. John Wiley & Sons.
Cruden, D.M., 1991. A simple definition of a landslide. Bull. Int. Assoc. Eng. Geol. 43 (1), 27–29.
Cruden, D.M., Varnes, D.J., 1996. Landslides: investigation and mitigation. Chapter 3-Landslide types and processes. Transp. Res. Board Spec. Rep. (247).
Dai, F., Lee, C., 2001. Frequency-volume relation and prediction of rainfall-induced landslides. Eng. Geol. 59 (3–4), 253–266.
Daniell, J.E., Schaefer, A.M., Wenzel, F., 2017. Losses associated with secondary effects in earthquakes. Front. Built Environ. 3. Article: 30.
Davison, A.C., Huser, R., 2015. Statistics of extremes. Annu. Rev. Stat. Appl. 2, 203–235.
Dowling, C.A., Santi, P.M., 2014. Debris flows and their toll on human life: a global analysis of debris-flow fatalities from 1950 to 2011. Nat. Hazards 71 (1), 203–227.
Dussauge, C., Grasso, J.-R., Helmstetter, A., 2003. Statistical analysis of rockfall volume distributions: implications for rockfall dynamics. J. Geophys. Res. Solid Earth 108 (B6).
Fan, X., Scaringi, G., Korup, O., West, A.J., van Westen, C.J., Tanyas, H., Hovius, N., Hales, T.C., Jibson, R.W., Allstadt, K.E., et al., 2019. Earthquake-induced chains of geologic hazards: patterns, mechanisms, and impacts. Rev. Geophys.
Farr, T.G., Rosen, P.A., Caro, E., Crippen, R., Duren, R., Hensley, S., Kobrick, M., Paller, M., Rodriguez, E., Roth, L., et al., 2007. The shuttle radar topography mission. Rev. Geophys. 45 (2).
Fell, R., 1994. Landslide risk assessment and acceptable risk. Can. Geotech. J. 31 (2), 262–272.
Fell, R., Corominas, J., Bonnard, C., Cascini, L., Leroi, E., Savage, W.Z., et al., 2008. Guidelines for landslide susceptibility, hazard and risk zoning for land-use planning. Eng. Geol. 102 (3–4), 99–111.
Fell, R., Harford, D., 1997. Landslide risk management. In: Cruden, D.M., Fell, R. (Eds.), Landslide Risk Assessment, Rotterdam Edition. Balkema, pp. 51–109.
Frattini, P., Crosta, G., Carrara, A., 2010. Techniques for evaluating the performance of landslide susceptibility models. Eng. Geol. 111 (1), 62–72.
Frattini, P., Crosta, G.B., 2013. The role of material properties and landscape morphology on landslide size distributions. Earth Planet. Sci. Lett. 361, 310–319.
Fuchs, S., Heiss, K., Hübl, J., 2007. Towards an empirical vulnerability function for use in debris flow risk assessment. Nat. Hazards Earth Syst. Sci. 7, 495–506.
Galli, M., Guzzetti, F., 2007. Landslide vulnerability criteria: a case study from Umbria, central Italy. Environ. Manag. 40 (4), 649–665, 00089.
Gelman, A., Carlin, J.B., Stern, H.S., Dunson, D.B., Vehtari, A., Rubin, D.B., 2013. Bayesian Data Analysis. CRC Press.
Giardini, D., Grünthal, G., Shedlock, K.M., Zhang, P., 1999. The GSHAP global seismic hazard map. Ann. Geophys. 42 (6).
Glade, T., Anderson, M., Crozier, M.J. (Eds.), 2005. Landslide Hazard and Risk, vol. 1. J. Wiley, Chichester, West Sussex, England; Hoboken, NJ. ISBN 978-0-471-48663-3.

Gneiting, T., Balabdaoui, F., Raftery, A.E., 2007. Probabilistic forecasts, calibration and sharpness. J. R. Stat. Soc. Ser. B (Stat. Methodol.) 69 (2), 243–268.
Gneiting, T., Genton, M.G., Guttorp, P., 2006. Geostatistical space-time models, stationarity, separability, and full symmetry. Monogr. Stat. Appl. Probab. 107, 151.
Grabs, T., Seibert, J., Bishop, K., Laudon, H., 2009. Modeling spatial patterns of saturated areas: a comparison of the topographic wetness index and a dynamic distributed model. J. Hydrol. 373 (1–2), 15–23.
GRASS Development Team, 2017. Geographic Resources Analysis Support System (GRASS) Software. Open Source Geospatial Foundation.
Gutenberg, B., Richter, C.F., 1936. Magnitude and energy of earthquakes. Science 83 (2147), 183–185.
Guthrie, R., Evans, S., 2004. Magnitude and Frequency of Landslides Triggered by a Storm Event. Loughborough Inlet, British Columbia.
Guzzetti, F., 2005. Landslide Hazard and Risk Assessment (Ph.D. Thesis). Mathematisch-Naturwissenschaftlichen Fakultät der Rheinischen Friedrich-Wilhelms-Universität. University of Bonn, Bonn, Germany, pp. 33–65.
Guzzetti, F., Ardizzone, F., Cardinali, M., Rossi, M., Valigi, D., 2009. Landslide volumes and landslide mobilization rates in Umbria, central Italy. Earth Planet. Sci. Lett. 279 (3–4), 222–229.
Guzzetti, F., Carrara, A., Cardinali, M., Reichenbach, P., 1999. Landslide hazard evaluation: a review of current techniques and their application in a multi-scale study, central Italy. Geomorphology 31 (1), 181–216.
Guzzetti, F., Galli, M., Reichenbach, P., Ardizzone, F., Cardinali, M., 2006. Landslide hazard assessment in the Collazzone area, Umbria, Central Italy. Nat. Hazards Earth Syst. Sci. 6 (1), 115–131.
Guzzetti, F., Malamud, B.D., Turcotte, D.L., Reichenbach, P., 2002. Power-law correlations of landslide areas in central Italy. Earth Planet. Sci. Lett. 195 (3–4), 169–183.
Guzzetti, F., Mondini, A.C., Cardinali, M., Fiorucci, F., Santangelo, M., Chang, K.-T., 2012. Landslide inventory maps: new tools for an old problem. Earth-Sci. Rev. 112 (1–2), 42–66.
Guzzetti, F., Reichenbach, P., Cardinali, M., Ardizzone, F., Galli, M., 2003. The impact of landslides in the Umbria region, central Italy. Nat. Hazards Earth Syst. Sci. 3, 469–486.
Guzzetti, F., Reichenbach, P., Cardinali, M., Galli, M., Ardizzone, F., 2005. Probabilistic landslide hazard assessment at the basin scale. Geomorphology 72 (1–4), 272–299.
Hansen, A., 1984. Landslide Hazard Analysis. Slope Instability. Wiley, New York, pp. 523–602.
Harp, E.L., Jibson, R.W., Schmitt, R.G., 2016. Map of landslides triggered by the January 12, 2010, Haiti earthquake. US Geol. Survey Sci. Investig. Map 3353, 15.
Heerdegen, R.G., Beran, M.A., 1982. Quantifying source areas through land surface curvature and shape. J. Hydrol. 57 (3–4), 359–373.
Hengl, T., de Jesus, J.M., Heuvelink, G.B., Gonzalez, M.R., Kilibarda, M., Blagotić, A., Shangguan, W., Wright, M.N., Geng, X., Bauer-Marschallinger, B., et al., 2017. SoilGrids250m: global gridded soil information based on machine learning. PLOS ONE 12 (2), e0169748.
Hengl, T., Kempen, B., Heuvelink, G., Malone, B., 2019. Package 'gsif'.
Hodges, J.S., 2013. Richly Parameterized Linear Models: Additive, Time Series, and Spatial Models Using Random Effects. CRC Press.
Hovius, N., Stark, C.P., Allen, P.A., 1997. Sediment flux from a mountain belt derived by landslide mapping. Geology 25 (3), 231–234.
Hrafnkelsson, B., Siegert, S., Huser, R., Bakka, H., Jóhannesson, A., 2020. Max-and-Smooth: A Two-Step Approach for Approximate Bayesian Inference in Latent Gaussian Models. Bayesian Analysis To appear.
Hungr, O., 1997a. Some methods of landslide hazard intensity mapping. In: Cruden, D. M., Fell, R. (Eds.), Landslide Risk Assessment, vol. 1. Balkema Publisher, Rotterdam, pp. 215–226.
Hungr, O., 1997b. Some methods of landslide hazard intensity mapping. Landslide Risk Assessment. Routledge, pp. 215–226.
Hungr, O., Leroueil, S., Picarelli, L., 2014. The Varnes classification of landslide types, an update. Landslides 11 (2), 167–194.
Jacobs, L., Dewitte, O., Poesen, J., Maes, J., Mertens, K., Sekajugo, J., Kervyn, M., 2017. Landslide characteristics and spatial distribution in the Rwenzori Mountains, Uganda. J. Afr. Earth Sci. 134, 917–930.
Jasiewicz, J., Stepinski, T.F., 2013. Geomorphons–a pattern recognition approach to classification and mapping of landforms. Geomorphology 182, 147–156.
Jeandet, L., Steer, P., Lague, D., Davy, P., 2019. Coulomb mechanics and relief constraints explain landslide size distribution. Geophys. Res. Lett. 46 (8), 4258–4266.
Jibson, R.W., Harp, E.L., Schulz, W., Keefer, D.K., 2004. Landslides triggered by the 2002 Denali Fault, Alaska, earthquake and the inferred nature of the strong shaking. Earthq. Spectra 20 (3), 669–691.
Jibson, R.W., R. Grant, A.R., Witter, R.C., Allstadt, K.E., Thompson, E.M., Bender, A.M., 2020. Ground failure from the anchorage, Alaska, Earthquake of 30 November 2018. Seismol. Res. Lett. 91 (1), 19–32.
Jibson, R.W., Tanyaş, H., 2020. The influence of frequency and duration of seismic ground motion on the size of triggered landslides-A regional view. Eng. Geol. 105671.
Jóhannesson, A., Siegert, S., Huser, R., Bakka, H., Hrafnkelsson, B., 2021. Approximate Bayesian Inference for Analysis of Spatio-Temporal Flood Frequency Data. Submitted, arXiv preprint:1907.04763.
Jordan, T., Marzocchi, W., Michael, A., Gerstenberger, M., 2014. Operational Earthquake Forecasting can Enhance Earthquake Preparedness.
Kargel, J.S., Leonard, G.J., Shugar, D.H., Haritashya, U.K., Bevington, A., Fielding, E., Fujita, K., Geertsema, M., Miles, E., Steiner, J., et al., 2016. Geomorphic and geologic controls of geohazards induced by Nepal's 2015 Gorkha earthquake. Science 351 (6269), aac8353.
Keefer, D.K., 1984. Landslides caused by Earthquakes. Geol. Soc. Am. Bull. 95 (4), 406–421.
Keefer, D.K., 2013. Landslides generated by Earthquakes: immediate and long-term effects. In: Shroder, J.F.JJr., Owen, L.A. (Eds.), Treatise on Geomorphology. Elsevier Ltd, San Diego, pp. 250–266.
Keefer, D.K., Manson, M.W., 1998. Regional distribution and characteristics of landslides generated by the earthquake. In: Keefer, D.K. (Ed.), The loma prieta, California, Earthquakes of October 17, 1989-landslides, pp. 7–32 u.s. geological survey professional paper(1551-c).
Kennedy, I., Petley, D., Williams, R., Murray, V., 2015. A systematic review of the health impacts of mass earth movements (landslides). PLOS Curr. 7 (DISASTERS).
Khaldoun, A., Moller, P., Fall, A., Wegdam, G., De Leeuw, B., Méheust, Y., Fossum, J.O., Bonn, D., 2009. Quick clay and landslides of clayey soils. Phys. Rev. Lett. 103 (18), 188301.
Khazai, B., Sitar, N., 2004. Evaluation of factors controlling earthquake-induced landslides caused by chi-chi earthquake and comparison with the northridge and loma prieta events. Eng. Geol. 71 (1–2), 79–95.
Kockelman, W.J., 1986. Some techniques for reducing landslide hazards. Bull. Assoc. Eng. Geol. 23 (1), 29–52.
Korup, O., Görüm, T., Hayakawa, Y., 2012. Without power? Landslide inventories in the face of climate change. Earth Surf. Process. Landf. 37 (1), 92–99.
Korup, O., Gorum, T., Hayakawa, Y.S., 2011. Without power? Landslide inventories in the face of climate change. Earth Surf. Process. Landf.
Krainski, E.T., Gómez-Rubio, V., Bakka, H., Lenzi, A., Castro-Camilo, D., Simpson, D., Lindgren, F., Rue, H., 2018. Advanced Spatial Modeling With Stochastic Partial Differential Equations Using R and INLA. Chapman and Hall/CRC.
Kramer, S.L., 1996. Geotechnical Earthquake Engineering. Prentice Hall, Upper Saddle River, N.J.
Kritikos, T., Robinson, T.R., Davies, T.R., 2015. Regional coseismic landslide hazard assessment without historical landslide inventories: a new approach. J. Geophys. Res. Earth Surf. 120 (4), 711–729.
Ksu, K.J., 1975. Catastrophic debris stream (Sturzstorm) generated by rockfalls. Geol. Soc. Am. Bull. 86, 129–140.
Lacroix, P., Zavala, B., Berthier, E., Audin, L., 2013. Supervised method of landslide inventory using panchromatic SPOT5 images and application to the earthquake-triggered landslides of Pisco (Peru, 2007, Mw8. 0). Remote Sens. 5 (6), 2590–2616.
Lagomarsino, D., Tofani, V., Segoni, S., Catani, F., Casagli, N., 2017. A tool for classification and regression using random forest methodology: applications to landslide susceptibility mapping and soil thickness modeling. Environ. Model. Assess. 22 (3), 201–214.
Lari, S., Frattini, P., Crosta, G., 2014. A probabilistic approach for landslide hazard analysis. Eng. Geol. 182, 3–14.
Larsen, I.J., Montgomery, D.R., Korup, O., 2010. Landslide erosion controlled by hillslope material. Nat. Geosci. 3 (4), 247.
Lombardo, L., Bakka, H., Tanyas, H., van Westen, C., Mai, P.M., Huser, R., 2019a. Geostatistical modeling to capture seismic-shaking patterns from earthquake-induced landslides. J. Geophys. Res. Earth Surf. 124 (7), 1958–1980.
Lombardo, L., Fubelli, G., Amato, G., Bonasera, M., 2016. Presence-only approach to assess landslide triggering-thickness susceptibility: a test for the Mili catchment (north-eastern Sicily, Italy). Nat. Hazards 84 (1), 565–588.
Lombardo, L., Mai, P.M., 2018. Presenting logistic regression-based landslide susceptibility results. Eng. Geol. 244, 14–24.
Lombardo, L., Opitz, T., Ardizzone, F., Guzzetti, F., Huser, R., 2020a. Space-time landslide predictive modelling. Earth-Sci. Rev. 103318.
Lombardo, L., Opitz, T., Huser, R., 2018a. Point process-based modeling of multiple debris flow landslides using INLA: an application to the 2009 Messina disaster. Stoch. Environ. Res. Risk Assess. 32 (7), 2179–2198.
Lombardo, L., Opitz, T., Huser, R., 2019b. Numerical recipes for landslide spatial prediction using R-INLA: a step-by-step tutorial. In: Pourghasemi, H.R., Gokceoglu, C. (Eds.), Spatial Modeling in GIS and R for Earth and Environmental Sciences. Elsevier, pp. 55–83. ISBN 978-0-12-815226-3.
Lombardo, L., Saia, S., Schillaci, C., Mai, P.M., Huser, R., 2018b. Modeling soil organic carbon with quantile regression: dissecting predictors' effects on carbon stocks. Geoderma 318, 148–159.
Lombardo, L., Tanyas, H., 2020. Chrono-validation of near-real-time landslide susceptibility models via plug-in statistical simulations. Eng. Geol. 278, 105818.
Lombardo, L., Tanyas, H., 2021. From scenario-based seismic hazard to scenario-based landslide hazard: fast-forwarding to the future via statistical simulations. Stoch. Environ. Res. Risk Assess. 1–14.
Lombardo, L., Tanyas, H., Nicu, I.C., 2020b. Spatial modeling of multi-hazard threat to cultural heritage sites. Eng. Geol. 105776.
MacMillan, R., Shary, P., 2009. Landforms and landform elements in geomorphometry. Dev. Soil Sci. 33, 227–254.
Malamud, B.D., Turcotte, D.L., Guzzetti, F., Reichenbach, P., 2004a. Landslides, earthquakes, and erosion. Earth Planet. Sci. Lett. 229 (1–2), 45–59.
Malamud, B.D., Turcotte, D.L., Guzzetti, F., Reichenbach, P., 2004b. Landslide inventories and their statistical properties. Earth Surf. Process. Landf. 29 (6), 687–711.
Marc, O., Hovius, N., Meunier, P., Gorum, T., Uchida, T., 2016. A seismologically consistent expression for the total area and volume of earthquake-triggered landsliding. J. Geophys. Res. Earth Surf. 121 (4), 640–663.
Marjanović, M., Kovačević, M., Bajat, B., Voženílek, V., 2011. Landslide susceptibility assessment using SVM machine learning algorithm. Eng. Geol. 123 (3), 225–234.

Martin, Y., Rood, K., Schwab, J.W., Church, M., 2002. Sediment transfer by shallow landsliding in the Queen Charlotte Islands, British Columbia. Can. J. Earth Sci. 39 (2), 189–205.
Massey, C., Townsend, D., Rathje, E., Allstadt, K.E., Lukovic, B., Kaneko, Y., Bradley, B., Wartman, J., Jibson, R.W., Petley, D., et al., 2018. Landslides triggered by the 14 november 2016 mw 7.8 kaikōura earthquake, New Zealandlandslides triggered by the 14 November 2016 mw 7.8 kaikōura earthquake, New Zealand. Bull. Seismol. Soc. Am. 108 (3B), 1630–1648.
Medwedeff, W.G., Clark, M.K., Zekkos, D., West, A.J., 2020. Characteristic landslide distributions: an investigation of landscape controls on landslide size. Earth Planet. Sci. Lett. 539, 116203.
Meunier, P., Hovius, N., Haines, A.J., 2007. Regional patterns of earthquake-triggered landslides and their relation to ground motion. Geophys. Res. Lett. 34 (20).
Mondini, A.C., Guzzetti, F., Chang, K.-T., Monserrat, O., Martha, T.R., Manconi, A., 2021. Landslide failures detection and mapping using Synthetic Aperture Radar: past, present and future. Earth-Sci. Rev. 216, 103574.
Nadim, F., Kjekstad, O., Peduzzi, P., Herold, C., Jaedicke, C., 2006. Global landslide and avalanche hotspots. Landslides 3 (2), 159–173.
National Research Council, 1991. A Safer Future. Reducing the Impacts of Natural Disasters. National Academy Press, Washington, D.C.. ISBN 978-0-309-04546-9.
Newhall, C.G., Self, S., 1982. The volcanic explosivity index (vei) an estimate of explosive magnitude for historical volcanism. J. Geophys. Res. 87 (C2), 1231–1238.
Nowicki, M.A., Wald, D.J., Hamburger, M.W., Hearne, M., Thompson, E.M., 2014. Development of a globally applicable model for near real-time prediction of seismically induced landslides. Eng. Geol. 173, 54–65.
Ohlmacher, G.C., 2007. Plan curvature and landslide probability in regions dominated by earth flows and earth slides. Eng. Geol. 91 (2), 117–134.
Parise, M., Jibson, R.W., 2000. A seismic landslide susceptibility rating of geologic units based on analysis of characteristics of landslides triggered by the 17 January, 1994 Northridge, California earthquake. Eng. Geol. 58 (3–4), 251–270.
Pelletier, J.D., Malamud, B.D., Blodgett, T., Turcotte, D.L., 1997. Scale-invariance of soil moisture variability and its implications for the frequency-size distribution of landslides. Eng. Geol. 48 (3–4), 255–268.
Pereira, S., Zêzere, J.L., Quaresma, I., 2017. Landslide societal risk in Portugal in the period 1865–2015. In: Workshop on World Landslide Forum, pp. 491–499.
Petley, D., 2012. Global patterns of loss of life from landslides. Geology 40 (10), 927–930.
Reichenbach, P., Galli, M., Cardinali, M., Guzzetti, F., Ardizzone, F., 2005. Geomorphologic Mapping to Assess Landslide Risk: Concepts, Methods and Applications in the Umbria Region of Central Italy. Landslide Risk Assessment. John Wiley, Chichester, pp. 429–468.
Reichenbach, P., Rossi, M., Malamud, B.D., Mihir, M., Guzzetti, F., 2018. A review of statistically-based landslide susceptibility models. Earth-Sci. Rev. 180, 60–91.
Rickli, C., Graf, F., et al., 2009. Effects of forests on shallow landslides-case studies in Switzerland. Forest Snow Landsc. Res. 82 (1), 33–44.
Roback, K., Clark, M., West, A., Zekkos, D., Li, G., Gallen, S., Godt, J., 2017. Map Data of Landslides Triggered by the 25 April 2015 Mw 7.8 Gorkha, Nepal Earthquake. US Geological Survey Data Release.
Roback, K., Clark, M.K., West, A.J., Zekkos, D., Li, G., Gallen, S.F., Chamlagain, D., Godt, J.W., 2018. The size, distribution, and mobility of landslides caused by the 2015 Mw7.8 Gorkha earthquake, Nepal. Geomorphology 301, 121–138.
Rossi, M., Cardinali, M., Fiorucci, F., Marchesini, I., Mondini, A.C., Santangelo, M., Ghosh, S., Riguer, D.E.L., Lahousse, T., Chang, K.-T., Guzzetti, F., 2012. A tool for the estimation of the distribution of landslide area in R. In: EGU General Assembly Conference | Geophysical Research Abstracts, vol. 14 pp. EGU2012-9438-1.
Rossi, M., Guzzetti, F., Salvati, P., Donnini, M., Napolitano, E., Bianchi, C., 2019. A predictive model of societal landslide risk in Italy. Earth-Sci. Rev.
Rossi, M., Witt, A., Guzzetti, F., Malamud, B.D., Peruccacci, S., 2010. Analysis of historical landslide time series in the emilia-romagna region, northern Italy. Earth Surf. Process. Landf. 35, 1123–1137.
Rue, H., Martino, S., Chopin, N., 2009. Approximate Bayesian inference for latent Gaussian models by using integrated nested Laplace approximations. J. R. Stat. Soc. Ser. B 71 (2), 319–392.
Rue, H., Riebler, A., Sørbye, S.H., Illian, J.B., Simpson, D.P., Lindgren, F.K., 2017. Bayesian computing with INLA: a review. Annu. Rev. Stat. Appl. 4, 395–421.
Saffir, H.S., 1973. Hurricane wind and storm surge. Mil. Eng. 423, 4–5.
Salvati, P., Bianchi, C., Rossi, M., Guzzetti, F., 2010. Societal landslide and flood risk in Italy. Nat. Hazards Earth Syst. Sci. 10, 465–483.
Salvati, P., Petrucci, O., Rossi, M., Bianchi, C., Pasqua, A.A., Guzzetti, F., 2018. Gender, age and circumstances analysis of flood and landslide fatalities in Italy. Sci. Total Environ. 610–611, 867–879.
Samia, J., Temme, A., Bregt, A., Wallinga, J., Guzzetti, F., Ardizzone, F., 2020. Dynamic path-dependent landslide susceptibility modelling. Nat. Hazards Earth Syst. Sci. 20 (1), 271–285.
Sappington, J.M., Longshore, K.M., Thompson, D.B., 2007. Quantifying landscape ruggedness for animal habitat analysis: a case study using bighorn sheep in the Mojave Desert. J. Wildl. Manag. 71 (5), 1419–1426.
Sassa, K., 1988. Speciallecture: geotechnical model for the motion of landslides. In: Proceedings 5th International Symposium on Landslides, Lausanne, vol. 1, pp. 37–55. Lausanne.
Šavrič, B., Patterson, T., Jenny, B., 2019. The Equal Earth map projection. Int. J. Geogr. Inf. Sci. 33 (3), 454–465.
Schabenberger, O., Gotway, C.A., 2017. Statistical Methods for Spatial Data Analysis. CRC Press.
Schmidt, K.M., Montgomery, D.R., 1995. Limits to relief. Science 270 (5236), 617–620.
Schmitt, R.G., Tanyas, H., Jessee, M.A.N., Zhu, J., Biegel, K.M., Allstadt, K.E., Jibson, R. W., Thompson, E.M., van Westen, C.J., Sato, H.P., Wald, D.J., Godt, J.W., Gorum, T., Xu, C., Rathje, E.M., Knudsen, K.L., 2017. An Open Rrepository of Earthquake-Triggered Ground-Failure inventories, vol. 1064. U.S. Geological Survey Data Series.
Shangguan, W., Hengl, T., de Jesus, J.M., Yuan, H., Dai, Y., 2017. Mapping the global depth to bedrock for land surface modeling. J. Adv. Model. Earth Syst. 9 (1), 65–88.
Simpson, R., 1974. The hurricane disaster potential scale. Weatherwise 27 (8), 169–186.
Soeters, R., Van Westen, C., 1996. Slope instability recognition, analysis and zonation. Landslides Investig. Mitig. 247, 129–177.
Soeters, R., van Westen, C.J., 1996. Slope instability recognition, analysis and zonation. In: Landslide Investigation and Mitigation, Number 247 in Transportation Research Board Special Report. National Research Council, Transportation Research Board, pp. 129–177.
Spiegelhalter, D.J., Best, N.G., Carlin, B.P., Van Der Linde, A., 2002. Bayesian measures of model complexity and fit. J. R. Stat. Soc. Ser. b (Stat. Methodol.) 64 (4), 583–639.
Stark, C., Guzzetti, F., 2009. Landslide rupture and the probability distribution of mobilized debris volumes. J. Geophys. Res. Earth Surf. 114 (F2).
Stark, C.P., Hovius, N., 2001. The characterization of landslide size distributions. Geophys. Res. Lett. 28 (6), 1091–1094.
Steger, S., Brenning, A., Bell, R., Glade, T., 2016. The propagation of inventory-based positional errors into statistical landslide susceptibility models. Nat. Hazards Earth Syst. Sci. 16 (12), 2729–2745.
Steger, S., Brenning, A., Bell, R., Glade, T., 2017. The influence of systematically incomplete shallow landslide inventories on statistical susceptibility models and suggestions for improvements. Landslides 14 (5), 1767–1781.
Steger, S., Mair, V., Kofler, C., Pittore, M., Zebisch, M., Schneiderbauer, S., 2021. Correlation does not imply geomorphic causation in data-driven landslide susceptibility modelling-benefits of exploring landslide data collection effects. Sci. Total Environ. 776, 145935.
Stepinski, T.F., Jasiewicz, J., 2011. Geomorphons-a new approach to classification of landforms. Proc. Geomorphometry 2011, 109–112.
Tang, C., Tanyas, H., van Westen, C.J., Tang, C., Fan, X., Jetten, V.G., 2019. Analysing post-earthquake mass movement volume dynamics with multi-source DEMs. Eng. Geol. 248, 89–101.
Tanyaş, H., van Westen, C., Allstadt, K., Nowicki, A.J.M., Görüm, T., Jibson, R., Godt, J., Sato, H., Schmitt, R., Marc, O., Hovius, N., 2017. Presentation and analysis of a worldwide database of earthquake-induced landslide inventories. J. Geophys. Res. Earth Surf. 122 (10), 1991–2015.
Tanyaş, H., Allstadt, K.E., van Westen, C.J., 2018. An updated method for estimating landslide-event magnitude. Earth Surf. process. Landf. 43 (9), 1836–1847.
Tanyaş, H., Lombardo, L., 2020. Completeness index for earthquake-induced landslide inventories. Eng. Geol. 264, 105331.
Tanyaş, H., Rossi, M., Alvioli, M., van Westen, C.J., Marchesini, I., 2019a. A global slope unit-based method for the near real-time prediction of earthquake-induced landslides. Geomorphology 327, 126–146.
Tanyaş, H., van Westen, C.J., Allstadt, K.E., Jibson, R.W., 2019b. Factors controlling landslide frequency-area distributions. Earth Surf. process. Landf. 44 (4), 900–917.
Taylor, D.W., 1948. Fundamentals of Soil Mechanics. John Wiley & Sons.
Taylor, F.E., Malamud, B.D., Witt, A., Guzzetti, F., 2018a. Landslide shape, ellipticity and length-to-width ratios. Earth Surf. Process. Landf. 43 (15), 3164–3189.
Taylor, F.E., Malamud, B.D., Witt, A., Guzzetti, F., 2018b. Landslide shape, ellipticity and length-to-width ratios. Earth Surf. Process. Landf. 43 (15), 3164–3189.
Townsend, K.F., Gallen, S.F., Clark, M.K., 2020. Quantifying near-surface rock strength on a regional scale from hillslope stability models. J. Geophys. Res. Earth Surf. 125 (7) e2020JF005665.
UNESCO Working Party On World Landslide Inventory, 1995. A suggested method for describing the rate of movement of a landslide. Bull. Int. Assoc. Eng. Geol. 52, 75–78.
Valagussa, A., Marc, O., Frattini, P., Crosta, G., 2019. Seismic and geological controls on earthquake-induced landslide size. Earth Planet. Sci. Lett. 506, 268–281.
Van Niekerk, J., Bakka, H., Rue, H., Schenk, L., 2019. New Frontiers in Bayesian Modeling Using the Inla Package in R. arXiv:1907.10426 (arXiv preprint).
Varnes and the IAEG Commission on Landslides and Other Mass-Movements, 1984. Landslide Hazard Zonation: A Review of Principles and Practice, 3. Natural Hazards, Series Paris: United Nations Economic, Scientific and Cultural Organization UNESCO, p. 63.
Wald, D.J., Quitoriano, V., Heaton, T.H., Kanamori, H., 1999. Relationships between peak ground acceleration, peak ground velocity, and modified mercalli intensity in California. Earthq. Spectra 15 (3), 557–564.
Wald, D.J., Quitoriano, V., Worden, C.B., Hopper, M., Dewey, J.W., 2012. USGS "Did You Feel It?" internet-based macroseismic intensity maps. Ann. Geophys. 54 (6).
Wan, J.-Z., Wang, C.-J., 2018. Expansion risk of invasive plants in regions of high plant diversity: a global assessment using 36 species. Ecol. Inform. 46, 8–18.
Watanabe, S., 2010. Asymptotic equivalence of bayes cross validation and widely applicable information criterion in singular learning theory. J. Mach. Learn. Res. 11 (Dec), 3571–3594.
Watanabe, S., 2013. A widely applicable Bayesian information criterion. J. Mach. Learn. Res. 14 (March), 867–897.
van Westen, C., Castellanos, E., Kuriakose, S., 2008. Spatial data for landslide susceptibility, hazard, and vulnerability assessment: an overview. Eng. Geol. 102 (3–4), 112–131.
Williams, J.G., Rosser, N.J., Hardy, R.J., Brain, M.J., Afana, A.A., 2018. Optimising 4-d surface change detection: an approach for capturing rockfall magnitude-frequency. Earth Surf. Dyn. 6 (1), 101–119.
Wood, H.O., Neumann, F., 1931. Modified mercalli intensity scale of 1931. Bull. Seismol. Soc. Am. 21 (4), 277–283.

Worden, C., Wald, D., 2016. ShakeMap manual online: technical manual, user's guide, and software guide. US Geol. Surv.
Xu, C., Xu, X., Shyu, J.B.H., 2015. Database and spatial distribution of landslides triggered by the Lushan, China Mw 6.6 earthquake of 20 April 2013. Geomorphology 248, 77–92.
Xu, C., Xu, X., Tian, Y., Shen, L., Yao, Q., Huang, X., Ma, J., Chen, X., Ma, S., 2016. Two comparable earthquakes produced greatly different coseismic landslides: the 2015 Gorkha, Nepal and 2008 Wenchuan, China events. J. Earth Sci. 27 (6), 1008–1015.
Zevenbergen, L.W., Thorne, C.R., 1987. Quantitative analysis of land surface topography. Earth Surf. process. Landf. 12 (1), 47–56.